Pliocene shorelines and the epeirogenic motion of continental margins: A target dataset for dynamic topography models

Andrew Hollyday[1], Maureen E. Raymo[1], Jacqueline Austermann[1], Fred Richards[2], Mark Hoggard[3], Alessio Rovere[4,5]

[1]Department of Earth & Environmental Sciences, Columbia University & Lamont-Doherty Earth Observatory, New York, USA
[2]Department of Earth Science & Engineering, Imperial College London, London, UK
[3]Research School of Earth Sciences, Australian National University, Canberra, AU
[4]Department for Environmental Sciences, Informatics and Statistics (DAIS), Ca' Foscari University of Venice, Venice, IT
[5]MARUM Center for Maine Environmental Services, Universität Bremen, Bremen, DE

Correspondence to: Andrew Hollyday (andrewh@ldeo.columbia.edu)

Abstract. Global mean sea level during the mid-Pliocene Epoch (~3 Ma), when CO_2 and temperatures were above present levels, was notably higher than today due to reduced global ice sheet coverage. Nevertheless, the extent to which ice sheets responded to Pliocene warmth remains in question, owing to high levels of uncertainty in proxy-based sea-level reconstructions as well as solid Earth dynamic models that have been used to evaluate a limited number of data constraints. Here, we present a global dataset of ten wavecut scarps that formed by successive Pliocene sea-level oscillations and which are observed today at elevations ranging from ~6 to 109 m above sea level. The present-day elevations of these features have been identified using a combination of high-resolution digital elevation models and field mapping. Using the MATLAB interface TerraceM, we extrapolate the cliff and platform surfaces to determine the elevation of the scarp toe, which in most settings is buried under meters of talus. We correct the scarp-toe elevations for glacial isostatic adjustment and find that this process alone cannot explain observed differences in Pliocene paleoshoreline elevations around the globe. We next determine the signal associated with mantle dynamic topography by back-advecting the present-day three-dimensional buoyancy structure of the mantle and calculating the difference in radial surface stresses over the last 3 Myr using the convection code ASPECT. We include a wide range of present-day mantle structures (buoyancy and viscosity) constrained by seismic tomography models, geodynamic observations, and rock mechanics laboratory experiments. Finally, we identify preferred dynamic topography change predictions based on their agreement with scarp elevations and use our most confident result to estimate a Pliocene global mean sea level based on one scarp from De Hoop, South Africa. This inference (11.6 ± 5.2 m) is a downward revision and may imply ice sheets were relatively resistant to warm Pliocene climate conditions. We also conclude, however, that more targeted model development is needed to more reliably infer mid-Pliocene global mean sea level based on all scarps mapped in this study.

1 Introduction

1

While projections of global mean sea level (GMSL) rise by 2050 show relatively good agreement with one another, they diverge significantly by 2100, spanning a range of <0.5 m to >2.5 m (DeConto et al., 2021; Masson-Delmotte et al., 2021).

35 This wide range reflects greater sensitivity of GMSL to factors such as the emission scenario and the mechanical processes that control ice-sheet stability (Masson-Delmotte et al., 2021). To reduce uncertainty in sea-level projections for 2100 and beyond, some studies have used ice-sheet models forced under paleoclimate conditions to identify which model parameters can reproduce melt responses consistent with sea-level constraints from the geologic past (DeConto et al., 2021; Edwards et al., 2019; Masson-Delmotte et al., 2021). As such, the confidence of near-future sea-level projections depends on the level of

40 confidence and uncertainty associated with sea-level change in the past.

The Pliocene Epoch (5.3 to 2.6 Ma), which consisted of a climate similar to present and projected conditions, may serve as a testing ground to better understand Earth's imminent climate future and has been widely used to calibrate dynamic ice-sheet models (Burke et al., 2018; DeConto et al., 2021; Dumitru et al., 2019). The Mid Pliocene Warm Period (MPWP; ~3.3 to 2.9 Ma), in particular, was characterized by maximum warm period temperatures 2.5°C to 4°C above the 1850 to 1900

45 baseline and had CO_2 concentrations close to modern values (~360 to ~420 ppm; Fedorov et al., 2013; Fischer et al., 2018; Haywood et al., 2013). Polar amplification was substantial as well with temperatures ~8°C above the 1850 to 1900 baseline in high-latitude regions (Fischer et al., 2018). While quantifying the melt response of ice sheets under these warm conditions can provide important model parameterization, to date, estimates of GMSL during the MPWP relative to present span a substantial range of ~5 to 25 m (Masson-Delmotte et al., 2021). For example, Dumitru et al. (2019) constrained GMSL between 5.6 m

50 and 19.2 m (16th and 84th percentiles) using phreatic overgrowth on speleothems from Mallorca, Spain, which date to 3.27 ± 0.12 Ma and were corrected for solid Earth deformation since their formation. Richards et al. (2023) also corrected for deformation of five circum-Australian MPWP paleo-sea level markers and constrained GMSL between 10.4 m and 21.5 m. These two studies are currently the only inferences for the MPWP that accounts for various Earth deformation processes and rigorously propagates and reports uncertainty; however, GMSL estimates from coastal features from South Africa (~14 m;

55 Hearty et al., 2020), the United States (~15 m; Moucha & Ruetenik, 2017), and New Zealand (~25 m; Grant et al., 2019) generally support this range.

Constraining GMSL millions of years back in time poses several distinctive challenges. While oxygen isotope-based sea-level reconstructions offer the advantage of being continuous through time, they consist of inherently high uncertainties (~10 to 13 m) due to ocean temperature effects, diagenetic processes, and unconstrained sea water chemistry (Grant et al.,

60 2014; Raymo et al., 2018; Rovere et al., 2014; Shakun et al., 2015; Spratt & Lisiecki, 2016). Alternatively, relic coastal features (i.e., paleoshorelines) along the margins of the global oceans outline past sea-level changes. By correcting for post-depositional effects such as sediment compaction, crustal deformation, glacial isostatic adjustment (GIA), and mantle dynamic topography (DT; i.e., surface deflections caused by mantle convection), one can constrain a GMSL offset from present day.

Models of GIA, a process that describes the viscoelastic response of the solid Earth, its gravity field, and rotation

65 axis, to changes in ice and ocean loads (Farrell & Clark, 1976), consist of uncertainties due to the ice-loading history and the mantle rheological structure. GIA models produce up to meters-scale uncertainties that are greatest in the near field and

smallest in the far field of ice-sheet loading. Simulations and observations of DT change suggest convection can cause surface deflections at rates as high as >100 m Myr^{-1} (Austermann et al., 2015; Czarnota et al., 2013; Guiraud et al., 2010; Hoggard et al., 2016; Hollyday et al., 2023; Roberts & White, 2010). As a result, ancient shorelines have undergone significant

70   spatiotemporally variable deformation due to DT change, even at passive margins, which were once thought to be relatively stable (Austermann et al., 2017; Moucha et al., 2008). However, uncertainties in these models are on the order of 10s to 100s of meters due the presence of many more free and unconstrained parameters associated with the mantle's rheological, viscosity, density, compositional, and temperature structure. Nonetheless, the epeirogenic motion of paleoshorelines can be corrected for using geodynamic predictions, revealing information about past ice-sheet and sea-level change from direct geologic evidence

75   (e.g., Hollyday et al., 2023; Moucha & Ruetenik, 2017).

Rovere et al. (2014) reported three wavecut escarpments from Australia, the United States, and the Republic of South Africa, which were all carved during Pliocene times by the continuous, low amplitude oscillations in sea level. These oscillations are inferred from the benthic $\delta^{18}O$ record, a climate proxy that shows ice volume and temperature always returned to approximately the same level over more than two million years of orbitally-paced climate cycles from approximately 5 Ma

80   to 3 Ma (Lisiecki & Raymo, 2005). After ~2.9 Ma, global ice volume expanded permanently due to the intensification of northern hemisphere glaciation, and GMSL would have retreated seaward, stranding these former sea cliffs inland. Late Pliocene intertidal to subtidal facies are found at the base of the scarps (Dowsett & Cronin, 1990; James et al., 2006; Rovere et al., 2014). This scarp formational process is consistent with simulations of marine terrace formation by Trenhaile (2014), particularly in settings where relatively slow uplift has occurred.

85   Here, we augment the initial Rovere et al. (2014) database consisting of three Pliocene scarps by including seven additional sites found using high-resolution topography data. We characterize the topography of each site using remotely sensed and, in some locations, direct field observations. These sites occur on continental margins characterized by a flat coastal plain bounded by a steeper scarp. In each case, the coastal plains extend for tens to hundreds of kilometers inland from the ocean and are mantled with late Pliocene to Pleistocene marine sediments that extend to the scarp "toe," or the intersection

90   between the scarp cliff and platform surfaces. Older, typically Miocene facies occur inland from the scarp toe (Fig. 1). These roughly shore-parallel scarps, which range from a few 10s of km to >1000 km in length, have all undergone some combination of erosion, uplift, subsidence, and isostatic adjustment since their formation. Here, we compare the observed elevations of these paleoshoreline features to predictions of GIA and DT (Raymo et al., 2011; Hollyday et al., 2023). The total vertical and along-scarp displacement of a shoreline from a horizontal, eustatically-controlled baseline provides constraint that allows us

95   to evaluate DT model output, information that ultimately will lead to the improvement of such models as well as the eventual isolation of a common Pliocene GMSL signal from a global observational database.

100
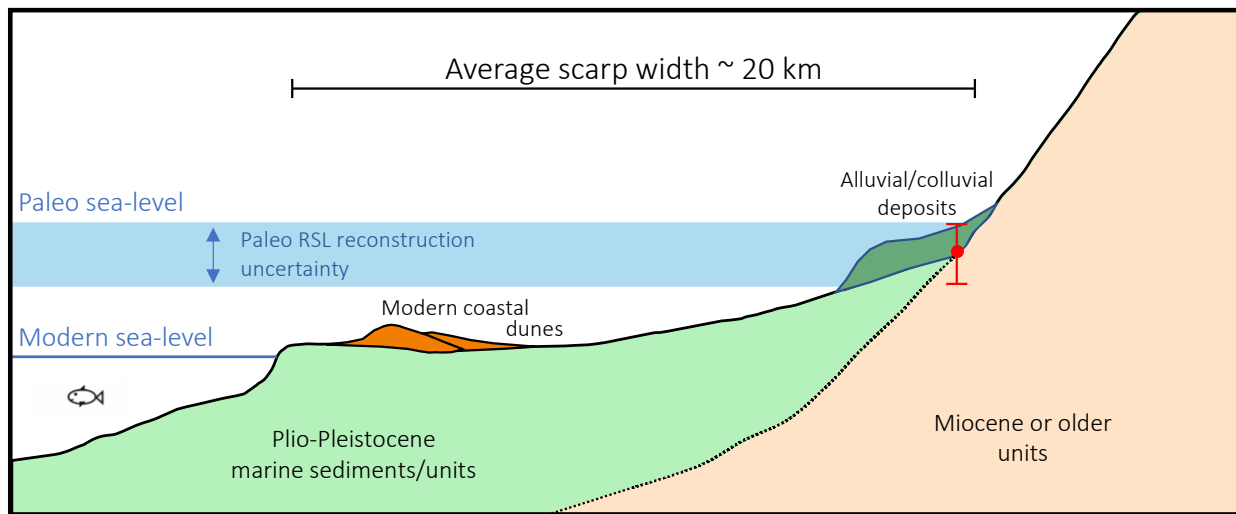
Figure 1: Schematic illustration of coast-perpendicular scarp profile. The grey lines (dashed lines indicate 2σ uncertainty bands) represent the TerraceM analysis, where the cliff and platform surfaces have been extrapolated to determine their geometric intersection, which often is buried under meters of alluvial/colluvial material (colored in dark green). The red point corresponds to the scarp toe elevation, and the red uncertainty bar describes the RSL estimate before the indicative range, GIA, or DT change corrections have been applied.

2 Methods

2.1 Initial search for Pliocene scarps

To guide a global search for Pliocene-aged scarps, we used the EarthEnv-DEM90 digital elevation model (DEM) dataset, which has a lateral resolution of 90 m (Robinson et al., 2014). Using the topographic modeling tool in the ENVI software package, we built a 1 arc-degree pixel-scale raster that represents land-surface slope on continental margins (<100 km from the sea). This tool compares elevation values across a 3 x 3-pixel grid. Note that since the surface slope is calculated from this grid, geomorphological features that have a lateral extent less than the pixel size of ~270-300 m are not resolved. From this slope map, we identified coastal plains that had low slopes indicative of long-term coastal erosion down to a marine platform. We chose a slope value of 0.625 (**m km**$^{-1}$) since this is lower than the average slope of the coastal plains located seaward of the three Pliocene scarps mapped in Rovere et al. (2014) and is also consistent with continental shelf clinoform angles as modeled by Pirmez et al. (1998). We then eliminated all locations where the general topography did not exhibit a relatively steep inland scarp with a high rim bounding the coastal plain. Additionally, any such slope breaks (e.g., scarp) that was less than 20 km in length was excluded in order to focus on longer wavelength topographic features, hypothesized to be paleoshorelines that can be used to assess long-term deformation of continental margins. We consider the toe of each scarp to represent a former sea-level highstand (Fig. 1). Our analysis includes only scarp/plain regions where independent literature

and/or geologic maps confirm that shallow marine sediments of Plio-Pleistocene age blanket the coastal plain. Finally, we classify the quality of each scarp's geochronology with qualitative descriptors: weak, moderate, or strong (Fig. 2). A weak

125   constraint lacks absolute and robust relative age control; a moderate constraint consists of a robust relative geochronology; and a strong constraint requires absolute age control. Classifying the formational age uncertainty of the scarps ultimately informs our data-model comparison as our geodynamic models do not explicitly account for this source of uncertainty. All age control qualifiers reflect an estimate of the confidence of the geochronology relative to mid-Pliocene times (3 Ma).
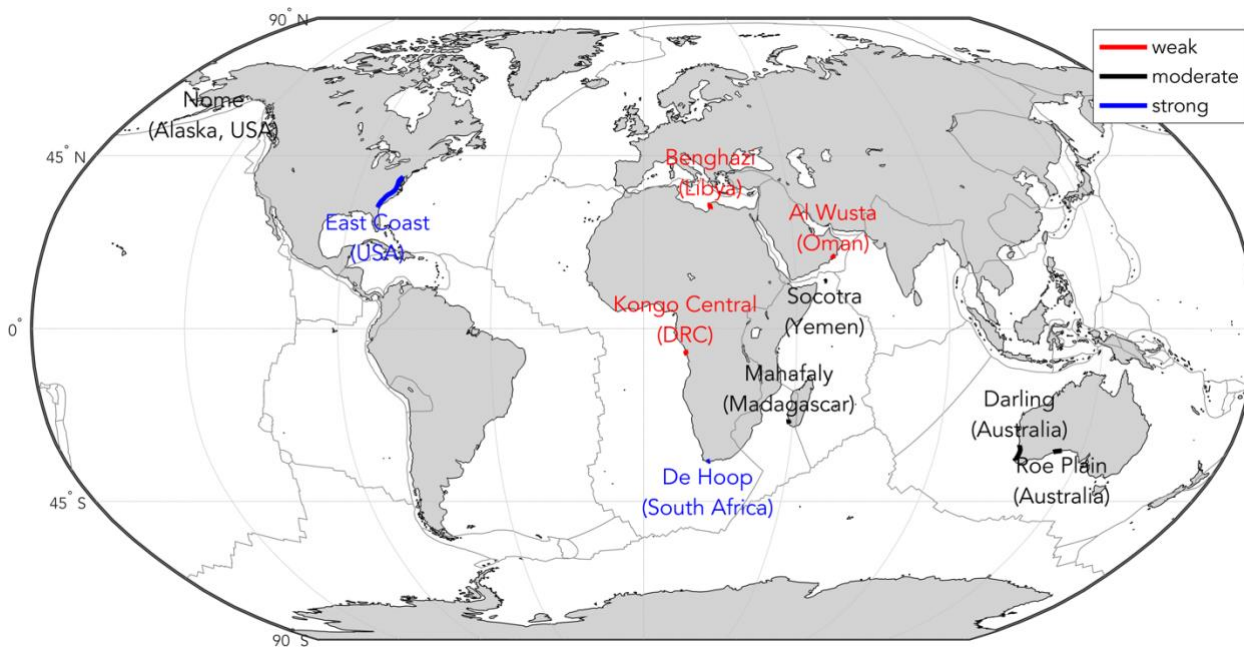

130   **Figure 2: Global compilation of ten Pliocene-aged scarps. Colors indicate the quality of the age constraint relative to the MPWP (3 Ma).**

2.2 High-resolution scarp mapping

Following the initial global search for Pliocene-aged scarps, we used higher resolution DEMs from the Shuttle Radar Topography Mission (SRTM) which is resolved at 1 arc-second (30 m; Farr et al., 2007). Vertical errors were assessed from

135   ground truthing and are <10 m globally, with the greatest uncertainties in places with high relief (Rodríguez et al., 2006, 2005). We note that the Nome (Alaska, USA) site was not analyzed in high resolution as SRTM data is not available at that latitude. Points were approximately chosen every 30 m (resolution of DEMs) along each scarp where a clear break in slope occurs. These points represent the approximate intersection of scarp cliff and platform surfaces, or the scarp toe (Fig. 1). Next, we defined profiles orthogonal to the scarp that pass through each point along the scarp to characterize the geomorphological

140   structure. Using the previously defined points, we visually selected the base of the escarpment cliffs and extracted the elevation. While this secondary procedure places a more precise constraint on remotely sensed elevations compared to the initial global

search, ongoing alteration of the surface geomorphology owing to stream incision, flexural and brittle crustal deformation, and colluvial/alluvial deposition are readily apparent in almost all the DEMs that we evaluate (Fig. 1 & 3). Given these factors, we assigned points away from regions clearly affected by stream incision and/or faulting, though these processes can be challenging to uniquely identify from DEMs. To constrain the extent to which colluvium has buried the scarp toes, we performed an additional analysis, which is described in Section 2.3. We did not quantitively consider the role that sedimentary loading changes may have had on isostatic and flexural deformation of the scarps; however, the GIA correction (Section 2.4.1) that we applied includes flexural deformation due to sea-level (or ice load) changes since the time of each scarp's initial formation.

150
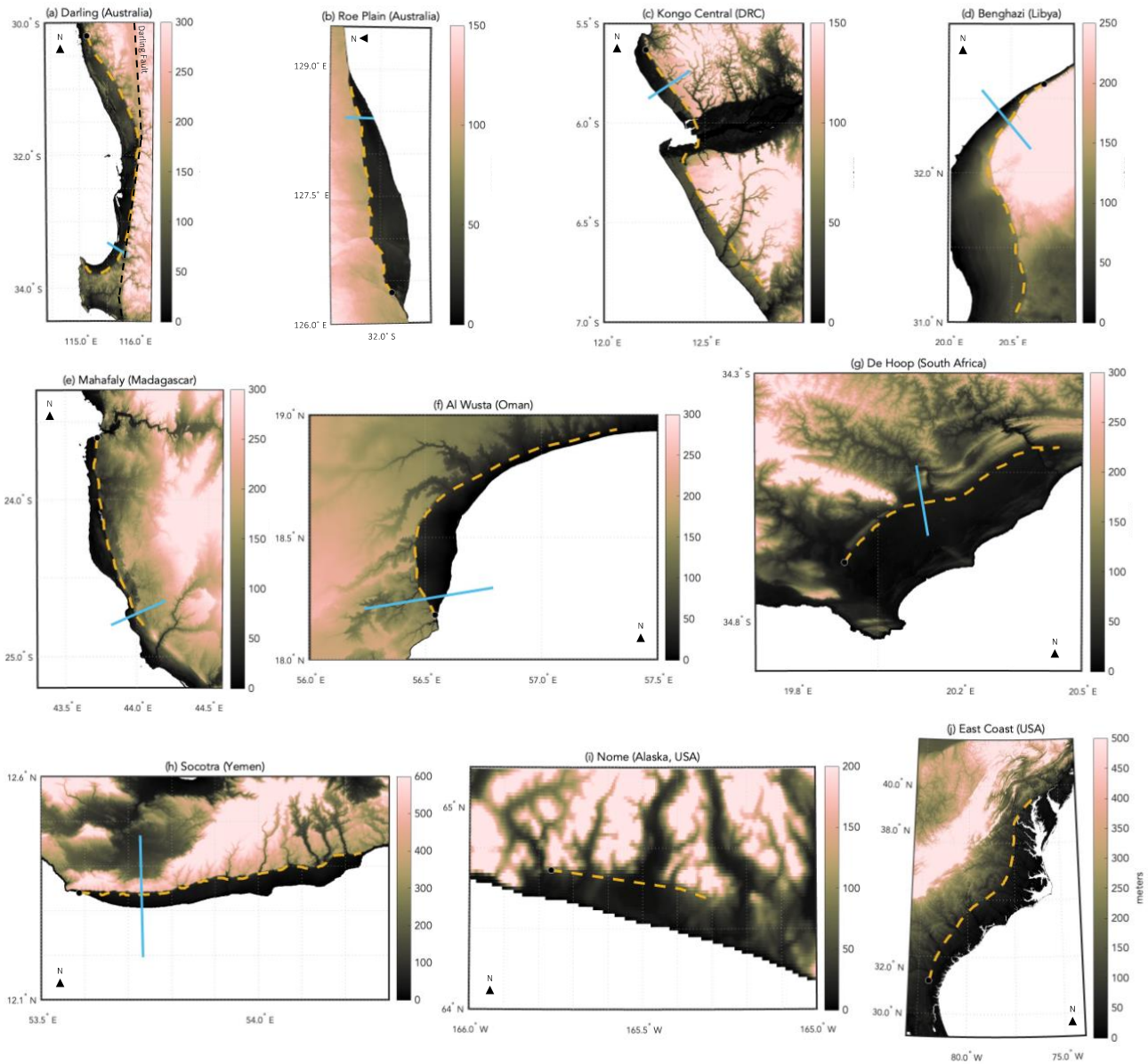
Figure 3: Compilation of DEMs for Pliocene-aged scarp database. (a-h): DEMs from the SRTM (Farr et al., 2007). (i & j): DEMs from the General Bathymetric Chart of the Oceans (GEBCO) 2023 grid (GEBCO Compilation Group, 2023). GEBCO DEMs were not used in our analysis of scarp geomorphology. Black circles indicate distance zero of the along-scarp profile, and the yellow dashed lines trace the along-scarp profile. Teal lines show the specific locations of the profiles perpendicular to the scarp, which were analyzed with TerraceM and are shown in Figure 4.

2.3 TerraceM mapping and indicative meaning

To determine the intersection between the scarps' cliff and platform surfaces, we employed the MATLAB interface
160 TerraceM, which is a tool developed to quantitatively assess how various surface processes have affected topographic evolution (Jara-Muñoz et al., 2016). We used TerraceM to determine the elevation of the scarp toe for each cross section defined orthogonal to the scarp. TerraceM identified maximum elevation profiles perpendicular to the scarp within a swath that was drawn over the previously assigned along-scarp points. The maximum elevation profile was used because this reflects the surface that has been eroded the least and likely corresponds to the most accurate depiction of paleo-sea level. Next, using
165 TerraceM, we computed linear regressions for each cliff and platform surface and extrapolated them to find their intersection, or the scarp toe, buried beneath alluvium or colluvium (Fig. 1). Vertical uncertainties of the intersection were computed from extrapolated 2σ ranges in the linear regressions (Jara-Muñoz et al., 2016). To note, only a small subset of elevation profiles showed paradigmatic geomorphology, with clearly defined cliff and platform surfaces. In most cases, the structure was more complex, reflective of multiple surface and neotectonic processes acting together. These include aeolian deposition (i.e.,
170 dunes), tectonic faulting, fluvial incision, and alluvial and colluvial deposition, and were important factors taken into consideration while defining the cliff and platform surfaces. Given the presence of surface deposition along many of the scarps, in almost all cases our TerraceM analysis adjusted elevations downward.

The TerraceM analysis allowed us to calculate at each point along the scarp profiles the elevation of the inner margin of the marine terrace (in some geographic areas referred to as the "shoreline angle," see Davis (1933) and Muhs (2022)), which
175 is commonly used as a proxy for former relative sea level. However, the relationship between the elevations of the inner margin (i.e., scarp toe) and the former sea-level position needs to be quantified through the calculation of the indicative meaning (Kelsey, 2015), which is defined by the reference water level and the indicative range (Rovere et al., 2016; Shennan, 2015; van de Plassche, 2013). These two elements define the position of the paleo-relative sea level with respect to the measured sea-level index point and associated uncertainty. In the absence of modern analogues (i.e., direct measurements of the inner
180 margin of modern coastal sites within the areas of interest), we adopted the values calculated by the software IMCalc (Lorscheid & Rovere, 2019) in each area. IMCalc calculates the reference water level and indicative range for a marine terrace at a given location by extracting local wave and tidal data. From these inputs, the highest reach of storm waves (storm wave swash height) and the breaking depth of ordinary waves are calculated and used as, respectively, upper and lower limits of the indicative range.

185 ### 2.4 Geodynamic models

2.4.1 Glacial isostatic adjustment

Each scarp was corrected for GIA following the approach of Raymo et al. (2011), which predicted disequilibrium due to both ongoing solid Earth, gravitational, and rotational adjustment from ice sheet variations since Marine Isotope Stage (MIS) 5e

(~122 ka) to present day as well as ice-sheet variations from the Pliocene Epoch (~3 Ma). Here, we only account for the former,

190 since they produce the larger signal and do not depend on assumptions about mid-Pliocene melt geometries. The time-evolving ice sheet geometries for the most recent disequilibrium (122 ka to present day) are from the ICE-5G model (Peltier, 2004), which was extended back to MIS 5e (see Raymo et al., 2011). While newer ice histories than ICE-5G have been published, most of the scarps are insensitive to the details of the ice history. The exceptions are scarps close to former ice sheets, for which a more detailed GIA analysis should be considered in future work. This correction uses 36 radial Earth structures that

195 consist of two lithospheric thicknesses (71 and 96 km), three (0.1×10^{21}, 0.3×10^{21}, 0.5×10^{21} Pa s) upper mantle viscosities, and six (3×10^{21}, 5×10^{21}, 7×10^{21}, 1×10^{22}, 2×10^{22}, and 3×10^{22} Pa s) lower mantle viscosities. While radial Earth structures neglect known lateral variations in mantle viscosity (e.g., Ritsema et al., 2011), we tested an ensemble of possible mantle structures to estimate the uncertainty (1σ) associated with an assumed 1-D structure. The final GIA correction is the mean and standard deviation of the ensemble.

2.4.2 Dynamic topography change

After correcting the elevations of each scarp for GIA, we compared the remaining deformation to a suite of DT change predictions based on models from Hollyday et al. (2023) and additional models parameterized with the TX2008 mantle structure (Simmons et al., 2009). To compute DT change over the last 3 Myr, we solved the governing equations for mantle convection, conservation of mass, energy, and momentum, and back-advected the present-day buoyancy structure of the mantle

205 using the finite element convection code ASPECT (Bangerth et al., 2020; Heister et al., 2017; Kronbichler et al., 2012). Using ASPECT 2.2.0, we ran global incompressible simulations (using the Boussinesq approximation) with surface and core-mantle-boundary (CMB) thermal boundary conditions set to 0˚C and 3027˚C, respectively. We set values for reference temperature (1333˚C), reference density (3300 kg m^{-3}), and specific heat (1250 J K^{-1} kg^{-1}). Depth-dependent gravity and thermal expansivity profiles were adopted from Glišović & Forte (2015), and thermal diffusivity was set to zero, since diffusion is not a time-

210 reversible process and is expected to be minimal over the timespan of 3 Myr. We did not include deflection of internal boundaries, thermal boundary layers, internal radiogenic heat production, or phase changes within our models. We paired three different radial viscosity profiles with nine different 3-D buoyancy structures to produce 27 total time-dependent simulations and accounted for lateral viscosity variations within our simulations through an Arrhenius relationship. Additional details of the model setup and parameters can be found in Hollyday et al. (2023).

215 The 3-D structure of the mantle is becoming increasingly well-resolved through seismic tomography (e.g., Lei et al., 2020; Schaeffer & Lebedev, 2013); however, subtle differences in the amplitude and extents of key structures occur across models. The initial tomography-derived buoyancy structure exerts a first-order influence on global convection styles and patterns of DT (Flament et al., 2013). To probe this uncertainty, we computed nine temperature models from shear-wave velocities. In the upper mantle, we computed temperatures from two high-resolution tomography models: GLAD-M25 and

220 SL2013sv (Lei et al., 2020; Schaeffer & Lebedev, 2013). Temperatures were computed using an experimentally and observationally constrained conversion that accounts for the anelastic behavior of the upper mantle (Richards et al., 2020;

Yamauchi & Takei, 2016). In the transition zone and lower mantle (below 410 km), we computed temperatures from four global tomography models: TX2011, GLAD-M25, S362ANI+M, and S40RTS (Grand, 2002; Lei et al., 2020; Moulik & Ekström, 2014; Ritsema et al., 2011). Using the linear, depth-dependent conversion factor from Steinberger (2016), we converted relative seismic velocities to relative density variations. We note that the choice of conversion factor directly influences the computed mantle buoyancy structure and while alternative conversions may be suitable, all lower mantle constraints are based on the same radially symmetric factor (except for the TX2008 model which is based on a joint seismic and geodynamic inversion). We combined each upper and lower mantle temperature structure to yield eight temperature fields. Additionally, we used the density field, TX2008, which is a joint inversion of geodynamic and seismic data (Simmons et al., 2009). The full conversion scheme for the construction of our initial temperature models, excluding those computed from the TX2008 density model (Simmons et al., 2009), is available in Supplementary Figure 1 of Hollyday et al. (2023). Following Jordan (1978), we assume the lithosphere is neutrally buoyant by correcting temperatures within the lithosphere to the depth average outside of the lithosphere. We perform this correction using tomography-specific maps of the lithosphere-asthenosphere boundary across the full model suite, except for the TX2008 model as cratonic structure was already accounted for within that joint inversion (Simmons et al., 2009). Our models also set a fixed lithospheric viscosity of 1×10^{22} Pa s (see Hollyday et al. (2023) for further details).

We computed DT from the radial surface stresses that result within our mantle convection simulations and the density contrast between the crust and overlying material (water or air; Zhong et al., 1993). To account for overburden changes from air to water along the coasts and over the ocean basins, we applied the formalism of Austermann & Mitrovica (2015) using a 90 km-thick lithosphere. We also computed perturbations to the Earth's geoid, as we are interested in sea-level change instead of just solid Earth deformation (geoid changes are included in "DT changes" for the remainder of the article). Displacement of DT fields over 3 Myr was accounted for with a plate motion correction, which is described in Hollyday et al. (2023). Our DT change predictions apply a no-net-rotation correction based on Argus et al. (2011) as well as a total lithospheric rotation based on Zheng et al. (2014). We explore total lithospheric rotation uncertainty by applying five different rotation values based on the mean value and the 1σ (0.195 and 0.305° Ma^{-1}) and 2σ (0.14 and 0.36° Ma^{-1}). This postprocessing procedure increases the total number of DT change predictions to 135.

To compare the data to model predictions, we first corrected observations for GIA and propagated uncertainties from GIA, elevation uncertainty, and indicative range. We then corrected each elevation for DT (one DT model at a time) and calculated a weighted mean GMSL and weighted standard deviation of GMSL for each site, where weights scale with the inverse of the uncertainty of each datapoint. If the uncertainty is small, it indicates that GIA- and DT-corrected scarp elevations form a mostly flat surface, which indicates that the DT prediction is more likely. The GMSL computed at any given point along a scarp is given by,

$$\text{GMSL}_{i,m} = \overline{\text{GE}_i} - \text{DT}_{i,m} \tag{1}$$

where the GIA-corrected elevation, $\overline{GE_i}$, is the observed elevation minus the GIA correction and $DT_{i,m}$ is the DT change prediction over 3 Myrs at the ith location along the scarp for model suite member, m. We compute single GMSL values at each scarp for every DT change model prediction as a weighted average, where the along-scarp weights, w_i, and resulting model-specific GMSL, $GMSL_m$, are given by,

$$w_i = 1 \Big/ \sigma^2_{GE_i} \tag{2}$$

$$GMSL_m = \frac{\sum_{i=1}^{N}(w_i \cdot GMSL_{i,m})}{\sum_{i=1}^{N} w_i}, \tag{3}$$

where σ_{GE_i} is the square root of the squared sums of the GIA, elevation measurement, and indicative range uncertainty at each location, i, along a given scarp and N is the total number of elevation measurements along a given scarp. We report the GMSL uncertainty as:

$$\sigma_{GMSL_m} = \sqrt{\frac{\sum_{i=1}^{N} w_i\left(GMSL_{i,m} - GMSL_m\right)^2}{\sum_{i=1}^{N} w_i}}, \tag{4}$$

where the weights are from Equation 2. Another way to quantify the success of a particular DT change model at reproducing along-scarp deformation is to calculate the mean squared weighted deviation (MSWD) of the GIA-corrected scarp elevations: the smaller the MSWD, the smaller the variability of GIA- and DT-corrected elevations and the higher the confidence in a specific DT model. The MSWD is given by,

$$MSWD_m = \frac{1}{N}\sum_{i=1}^{N}\left[\frac{\left(GMSL_{i,m} - GMSL_m\right)^2}{\sigma^2_{GE_i}}\right]. \tag{5}$$

We segregated DT change models into two groups, based on (1) weak MSWD (<30) and GMSL (0 m to 50 m) and (2) stringent MSWD (<20) and GMSL (10 m to 40 m) thresholds. The stringent thresholds were chosen with the goal of identifying models that have a high level of agreement with the observations and fall within existing constraints of Pliocene GMSL.

3 Results

We identified seven linear geomorphic features where an abrupt break in slope marks the transition between Plio-Pleistocene and older, inland rocks. These seven scarps are in addition to the three described in Rovere et al. (2014) and Rovere et al. (2015) to a make a total of ten in the dataset. See Supplementary Figure 1 for reported scarp elevations, indicative range, GIA correction, and the data source specific to each location. Each of the ten scarps described here exhibits short to long-wavelength patterns of solid Earth deformation that have evolved over millions of years. We have detailed this observed deformation in the context of each respective local geologic and geomorphic setting. Next, we have corrected the observed deformation of the scarps for GIA and compared the remaining deformation to a subset of preferred DT change models (those that pass the weak and stringent thresholds).

11

3.1 Scarp geomorphology

3.1.1 Darling (Australia)

The Darling (Australia) scarp is located in Western Australia (Fig. 2). The coastal plain is covered by Quaternary sediments of the Kwinana Group. The Bassendean Sands occur within this group and have been attributed to estuarine, shallow marine, and fluvial depositional environments. At the base of the scarp, the Yoganup Formation is characterized as a shoreline facies (Kendrick et al., 1991). In the northeast, the north-south trending Darling Fault divides these sedimentary units from the Darling plateau, where Archean to Cenozoic metamorphic and intrusive bodies occupy the higher elevation terrain (Raymond et al., 2012). The scarp coincides with the Darling Fault in its central part but diverges from it to the north and south (Fig. 3a). Several alluvial fans cover the scarp's toe, and four major rivers incise the paleoshoreline (Moore, Swan, Canning, and Brunswick Rivers). Absolute age control has not been established for this scarp, but the paleoshoreline is straddled by rock units that predate and postdate Pliocene times (Kendrick et al., 1991). As such, we classify its age control as moderate (Fig. 2). Remotely sensed elevations mapped in high resolution and analyzed with TerraceM (Fig. 4a) show short-wavelength patterns of deformation varying from 30 m to 105 m above present sea level along the length of the roughly north-south trending scarp. From north to south, elevations increase until ~70 km distance, before decreasing to the minimum mapped elevation at ~300 km distance; from ~300 km to the southern terminus of the scarp (469 km distance), elevations increase modestly (~15 m to 20 m; Fig. 5a).
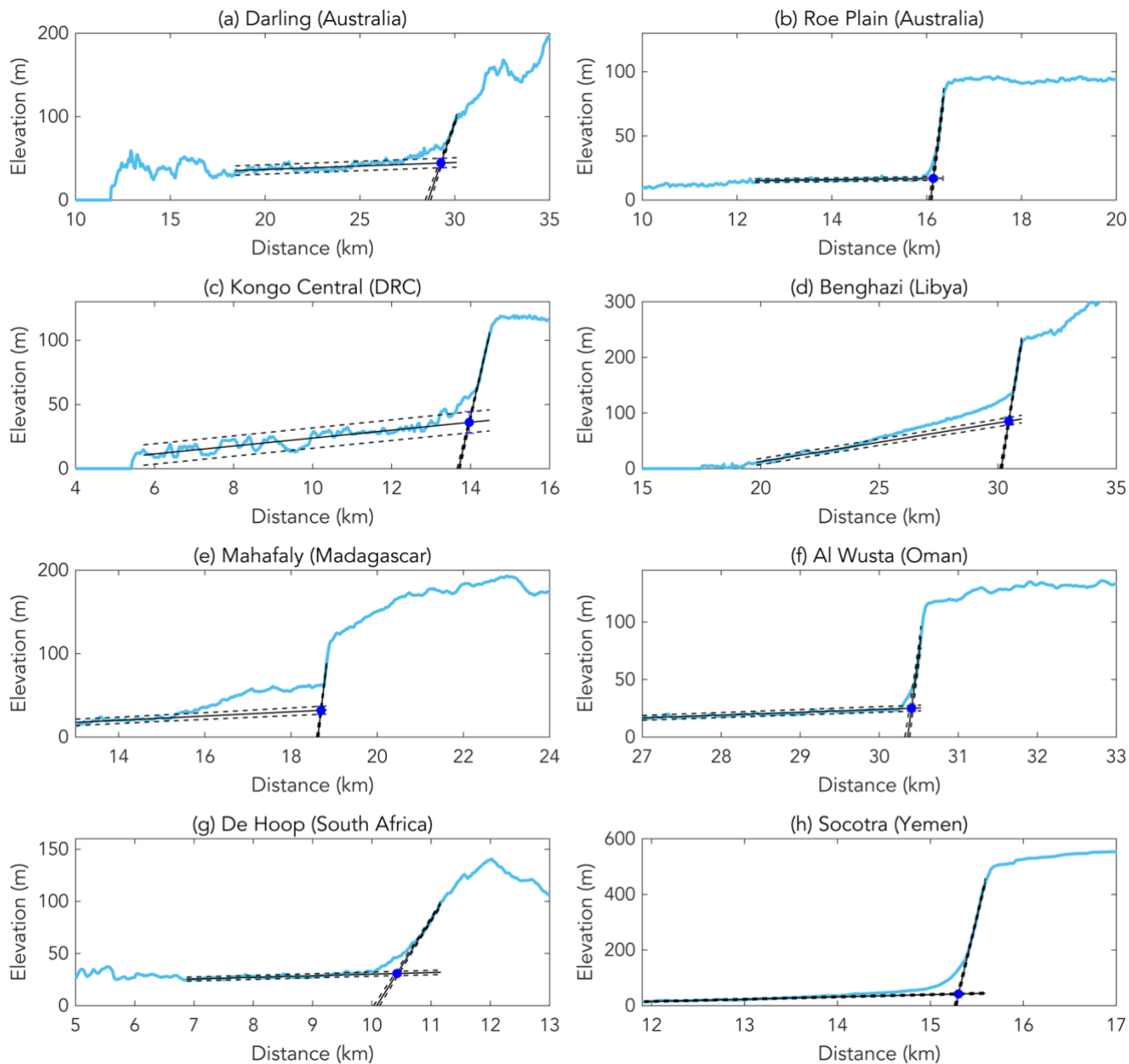
Figure 4: Scarp-perpendicular elevation profiles analyzed with TerraceM (Jara-Muñoz et al., 2016). Locations of each scarp are shown as teal profiles in Figure 3a-h. The black solid and dashed lines show the extrapolated platform and cliff surfaces and their 2σ uncertainties, respectively. The blue points correspond to the extrapolated intersection of the two surfaces.
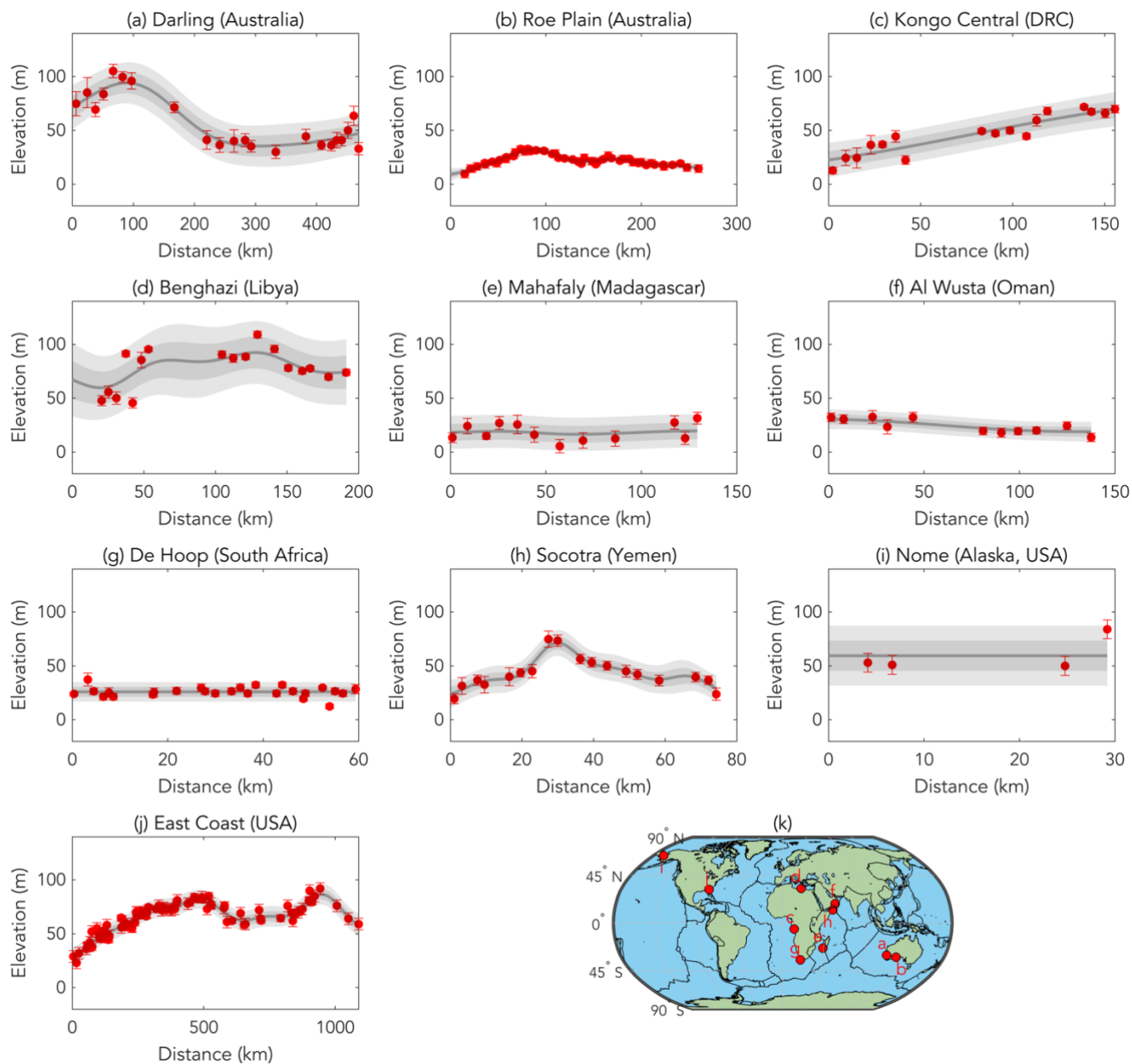
Figure 5: Along-scarp elevations profiles without geodynamic corrections. Red points indicate the mapped elevations of each scarp with uncertainties associated with the TerraceM analysis (Jara-Muñoz et al., 2016), field measurements, and indicative range. Gray line shows Gaussian Process Regression model trained by the data. Dark and light gray bands correspond to 1σ and 2σ uncertainties of the model, respectively. (a) Darling (Australia); (b) Roe Plain (Australia); (c) Kongo Central (DRC); (d) Benghazi (Libya); (e) Mahafaly (Madagascar); (f) Al Wusta (Oman); (g) De Hoop (South Africa); (h) Socotra (Yemen); (i) Nome (Alaska, USA); (j) East Coast (USA); (k) map inset showing site locations.

14

3.1.2 Roe Plain (Australia)

The Roe Plain (Australia) scarp, also known as the Hampton Escarpment, is located in Western Australia near the Great Australian Bight (Fig.3). The scarp's bedrock geological and geomorphological structure, which consists of Cenozoic limestone at the cliff and a Plio-Pleistocene shallow marine assemblage at the platform (James & Bone, 2007), is described in detail in Rovere et al. (2014). We characterize this scarp, which has been observed in the field (Rovere et al., 2014), with moderate age control due to the availability of a robust relative geochronology (Fig. 2). The Roe Plain (Australia) scarp is mapped with a combination of high-resolution remote sensing, TerraceM analysis (Fig. 4b), and direct field measurements. It extends 260 km in length and varies from 9.5 m to 32.8 m in elevation. The western beginning of the scarp trace marks its lowest point; from there elevations increase until ~75 km distance, where the maximum elevation occurs. From ~75 km to ~260 km distance, the elevations gradually decrease by ~20 m (Fig. 5b). Colluvial deposition at the scarp's toe is corrected for with our TerraceM analysis with corrections typically <10 m (Fig. 4b).

3.1.3 Kongo Central (DRC)

The Kongo Central scarp occurs along the Atlantic coast on the border of the Democratic Republic of the Congo (DRC) and Angola and is dissected by the Congo River, which is the second largest river in the world and has an average discharge of 45,000 $m^3 s^{-1}$ (Fig. 3c; Eisma & Van Bennekom, 1978). Nairn & Stehli (1982) describe the scarp's geology as Precambrian and Cretaceous in age, covered by Plio-Pleistocene sedimentary units. They report two to three marine terraces assumed to have formed over Pleistocene sea-level oscillations, though the structure of these terraces remains enigmatic from DEM mapping (Fig. 3c). As only a relative geochronology is available for this site, the age constraint of this scarp is characterized as weak (Fig. 2). The elevations of the Kongo Central (DRC) scarp, which are mapped in high resolution and analyzed with TerraceM, show a mostly linear increase along the length of the scarp (155.6 km; Fig. 5c) with minimum and maximum elevations estimates of 12.7 m to 71.8 m, respectively.

3.1.4 Benghazi (Libya)

The Benghazi (Libya) coastal plain is located along the northeastern coast of Libya, the eastern coast of the Gulf of Sirte, and the western margin of the Cyrenaica platform and the Jabal Al Akhdar uplift area (Fig. 3d; Fiduk, 2009). The capital city of Benghazi is situated on this coastal plain approximately 25 km to the west of the scarp. The Cyrenaica platform and Jabal Al Ahkdar bedrock, which compose the high elevation cliff terrain of the Benghazi (Libya) scarp are of Miocene and upper Cretaceous age, respectively (Hallett, 2002). The scarp is interrupted by a large colluvial deposit in its central part (Figs. 3d & 4d). The coastal plain consists of Pliocene sandstone with ichnofacies suggestive of a lower intertidal to shallow subtidal depositional environment (Kumar, 2015). We note that while these coastal plain sediments have been interpreted to be of Pliocene age, uncertain stratigraphic correlations for Quaternary and Pliocene units (Tawadros, 2001, 2011) as well as the

absence of absolute age constraints have led to age control that can generally be characterized as weak (Fig. 2). The elevations of the Benghazi (Libya) scarp are mapped in high resolution and analyzed with TerraceM (Fig. 4d). The full length of the scarp is ~191 km, beginning close to the coast (~8 km) in the north and extending inland as far as ~50 km in the south. The scarp is

345 characterized by considerable (~50 m, vertically) short-wavelength (10s of km, spatially) variability (Fig. 5d). The northernmost mapped elevations are as low as 45.6 m, and to the south the scarp's elevations increase to its maximum elevation at ~130 km distance (109.1 m elevation) before decreasing modestly until the terminus of the scarp trace in the south. Given the presence of well-developed colluvial and/or alluvial structures along the scarp's toe, the TerraceM analysis, which is well suited for this site, adjusts the scarp's elevations downwards by ~20 to 30 m (Fig. 4d).

350 ### 3.1.5 Mahafaly (Madagascar)

The Mahafaly (Madagascar) scarp is located in the southwest of Madagascar and borders the Mahafaly plateau to the east and a broad coastal plain to the west (Fig. 3e). Lake Tsimanampetsotsa occurs adjacent to the scarp ~55 km distance from the north. According to state geological maps, the surface sediments on this coastal plain are mostly composed of unconsolidated sands of Quaternary age (Dandouau, 1922; Nairn & Stehli, 1982; Persits et al., 1997). A preliminary field survey of the scarp

355 surroundings confirms that along the coastal plain, the bedrock consists of sub-horizontal shallow-marine, shell-rich limestone (Fig. 6). This scarp is marked by a lithological contact between the platform and cliff rocks with the cliff consisting of Tertiary limestones, marls, and chalks (Moat & Du Puy, 2010). Several dune fields occur across the coastal plain and adjacent to the scarp's toe in the south. While we lack an absolute geochronology for this site, the approximate relative chronology provides a moderate constraint on the scarp's age (Fig. 2). The elevations of the Mahafaly (Madagascar) scarp are mapped in high

360 resolution and analyzed with TerraceM (Fig. 4e). In total the scarp extends ~129 km and ranges in elevation from 5.5 m to 31.5 m, with its minimum and maximum elevations occurring in the scarp's center (~56 km distance) and southern terminus (~129 km distance), respectively. The mapped deformation is characterized by a slight downward dip in elevation at its center with higher elevations to the north and south (Fig. 5e).

16

Figure 6: Field photos from Mahafaly (Madagascar) scarp. (a): View from the top of the cliff, looking seawards. (b): Sub-horizontal limestone at the base of the scarp. (c): Limestone at the top of the Mahafaly cliff. (d): Detail of the shell-rich limestone outcrop on the coastal plain, between the inner margin of the scarp and the coast.

3.1.6 Al Wusta (Oman)

The Al Wusta (Oman) scarp is located in the Al Wusta governorate along the southern coast of Oman (Fig. 3f). This site lies to the south of the Hugf-Haushi Uplift and to the east of the South Oman Salt Basin (Grosjean et al., 2009; Robertson et al., 1990). Reverse faults and synclinal structures, that formed during Tertiary times, occur to the north and south of the scarp (Abbasi et al., 2013; Fournier et al., 2004; Hanna, 1990; Ries & Shackleton, 1990). The coastal plain sediments are classified as Quaternary in age, and the bedrock that composes the scarp cliff and elevated plateau are of Miocene or older origin (Fournier et al., 2004; Nairn & Stehli, 1982; Platel et al., 1994). Two large alluvial fans disrupt the trace of the scarp toe at the Wadi Ainina and Wadi Watif. With the lack of an absolute or robust relative age chronology, we classify this scarp as weak (Fig. 2). The Al Wusta (Oman) scarp has been mapped in high resolution and analyzed with TerraceM (Fig. 4f). The full length of the scarp extends ~138 km and varies in elevation from 13.7 m to 32.6 m. Given the presence of large alluvial and colluvial structures across the scarp, our TerraceM analysis provides significant improvement to our elevation estimates with downward corrections on the order of 10s of meters (Fig. 4f). This scarp exhibits a slight decrease in elevation from ~30 m in the south to ~20 m in the north, which mostly occurs between distance 40 km and 80 km (Fig. 5f).

3.1.7 De Hoop (South Africa)

The De Hoop (South Africa) scarp is located on the southern coast of the Republic of South Africa, ~160 km southeast of Cape Town (Fig. 3g). The coastal plain consists of the De Hoopvlei Formation (shallow water depositional environment; Malan, 1991). An oyster shell within the unit dates (Strontium Isotope Stratigraphy; SIS) to 3.56 ± 1.08 Ma and confirms this biostratigraphic correlation (Rovere et al., 2014). Further details on the geology, geomorphology, and structure of this scarp are found in Rovere et al. (2014). Given the availability of SIS geochronology, we classify the age control of this scarp as strong (Fig. 2). The De Hoop (South Africa) scarp is mapped with a combination of high-resolution remote sensing, TerraceM analysis, and direct field measurements. In total, the scarp extends ~59 km and varies from 12.4 m to 37.4 m in elevation (Fig. 5g). Lacking a clear, first-order pattern of short-wavelength variability, the toe of the De Hoop (South Africa) scarp occurs at ~28 m with consistent (but small) variability above and below this elevation across its full length. Due to the presence of colluvial deposition along the scarp's toe, our TerraceM analysis provides important downward correction on the order of ~10 m (Fig. 4g).

3.1.8 Socotra (Yemen)

The Socotra (Yemen) scarp is located on the island of Socotra ~360 km off the coast of mainland Yemen; the scarp is situated on the island's southern coast (Fig. 3h). The coastal plain consists of Plio-Quaternary sedimentary units that are interrupted by the limestone-dominated Eocene upland with a sharp cliff (Beydoun & Bichan, 1969; Pik et al., 2013). The Pliocene coastal plain sediments consist of horizontal terraces with conglomerate beds of marine fossils overlying older bedrock (Beydoun & Bichan, 1969). Schlüter (2006) describes prominent alluvial, colluvial, talus, dune, and beach deposits along the southern coast of Socotra, bordered to the north by Cretaceous limestones and marls. Several rivers dissect the scarp along its ~75 km length (Fig. 3h). We characterize this scarp as having moderate age control due to the availability of geologic maps but the lack of absolute dates (Fig. 2). Although the island of Socotra had undergone the majority of its post-rift adjustment by Miocene times following its separation from Arabia, this site represents one of the most dynamic tectonic settings included in this dataset, as it is situated proximal to the seismically active Arabia-India-Somalia triple junction (Birse et al., 1997; Fournier et al., 2001, 2010). The Socotra (Yemen) scarp, which is mapped in high resolution and analyzed with TerraceM (Fig. 4h), is characterized by a pattern of short-wavelength variability (~50 to 70 km, spatially). The maximum scarp elevation occurs at ~25 km distance at 74.9 m, after increasing from its lowest point (19.6 m) at start of the scarp trace to the west. The elevations descend gradually from the maximum elevation to the end of the trace (east), where elevations return to ~26 m (Fig. 5h).

3.1.9 Nome (Alaska, USA)

The Nome (Alaska, USA) scarp is located on the southern coast of the Seward Peninsula in Alaska (Fig. 2). The town of Nome is situated on the coast facing the Bering Sea, ~4 km from the scarp. The coastal plain is covered with glacial and

undifferentiated deposits, the latter of which is likely sourced from unglaciated uplands and lowlands (Péwé, 1975). Glaciation from MIS 6 likely extended to the Nome coastal plain; however, multiple sea-level highstands from late Pliocene to Pleistocene times also left imprints on the coastal plain (Kaufman & Brigham-Grette, 1993). The high elevation terrain that composes the scarp cliff rocks include Devonian to Ordovician schist and marble (Till et al., 2009). The oldest marine deposits mapped on the coastal plain are linked to the Beringian transgression (2.7 to 2.5 Ma). We characterize this scarp with moderate age control as the site has been well-mapped, and the relative geochronology provides a more robust constraint in comparison to other sites (Fig. 2). Due to a lack of SRTM coverage above 60˚N, the Nome (Alaska, USA) scarp was mapped in lower resolution and was not analyzed with TerraceM. Extending ~29 km in length, the Nome scarp varies in elevation from 50.0 m to 84.0 m. The mapped elevations remain relatively constant (~50 m) along the length of the scarp, then increase at the eastern margin of the scarp trace to 84.0 m (Fig. 5i).

3.1.10 East Coast (USA)

The East Coast (USA) scarp, also known as the Orangeburg Scarp, represents the longest and most studied scarp in this dataset (Fig. 2; e.g., Dowsett & Cronin, 1990; Rovere et al., 2014, 2015; Winker & Howard, 1977). To the south, the scarp's coastal plain is composed of the Duplin Formation, a warm, shallow marine and inner to middle-shelf facies. To the north, the plain consists of the Raysor Formation, which corresponds to a slightly deeper marine depositional environment (Huddlestun, 1988). Further details on the this scarp's geology, geomorphology, and structure can be found in Rovere et al. (2014) and Rovere et al. (2015). Given the presence of SIS ages (2.30 Ma to 3.57 Ma; Graybill et al., 2009; McGregor et al., 2011) and well-developed biostratigraphic constraints (e.g., Dowsett & Cronin, 1990), we classify this scarp's age confidence as strong (Fig. 2). The East Coast (USA) scarp is mapped in high resolution and with direct field measurements. A TerraceM analysis was not performed for this site since it has been extensively mapped based on DEMs and field observations as described in Rovere et al. (2015). Along its 1089 km length, this scarp exhibits long-wavelength patterns of variability with elevations ranging between 23.0 m and 92.0 m. From south to north, the East Coast (USA) scarp increases in elevation until ~520 km distance to ~80 m, before decreasing modestly (by ~30 m) until ~660 km distance (Fig. 5j). The scarp then increases again to its maximum point ~925 km distance and decreases again by ~25 m for another ~160 km distance to the northern terminus of the scarp (Fig. 5j).

3.2 GIA correction

The Nome (Alaska, USA) site is most significantly affected by GIA, with a mean (mean of the mean and mean of the standard deviation across Earth models) of 6.39 ± 0.11 (1σ) m, as it is located on the actively subsiding peripheral bulge of the former Laurentide Ice Sheet. The East Coast (USA) scarp is also affected by ongoing solid Earth adjustment from the collapsed Laurentide Ice Sheet, with a mean correction of 3.33 ± 4.69 (1σ) m along the scarp trace. At this site, the correction transitions from positive to negative moving north along the scarp, which is a result of peripheral bulge subsidence in the south and solid

Earth rebound in the north (Fig. 7a). These two sites will be most sensitive to the ice history chosen in the GIA correction, which is not varied in this study. All of the remaining sites are located in the far field of ice loading changes and have corresponding GIA corrections characterized by lower uncertainty (Fig. 7b). Continental levering, a mechanism that occurs

445   due to loading and unloading of water on the continental shelf and the flexural response of the lithosphere along coastlines, is the primary driver of adjustment at the remaining sites. Mean corrections and 1σ uncertainties at the Kongo Central (DRC; -3.9 ± 0.03 m), De Hoop (South Africa; -2.26 ± 0.05 m), Mahafaly (Madagascar; -1.20 ± 0.10 m, Benghazi (Libya; -1.17 ± 0.53 m), Al Wusta (Oman; -3.92 ± 0.08 m), Socotra (Yemen; -2.36 ± 0.07 m), Darling (Australia; -0.22 ± -0.61 m), and Roe Plain (Australia; -2.50 ± 0.12 m) sites also have minor contributions from perturbations to Earth's rotation axis (e.g., Australian

450   sites) and equatorial syphoning (e.g., Kongo Central site), which occurs when local sea level falls in response to distal infilling of subsiding peripheral bulges. At all sites, the GIA correction does not fully account for the amplitude of observed elevations or the spatial elevation variability of the mapped scarps (Figs. 7a & 8), and ultimately it is a minor contributor to scarp elevation in comparison to DT.
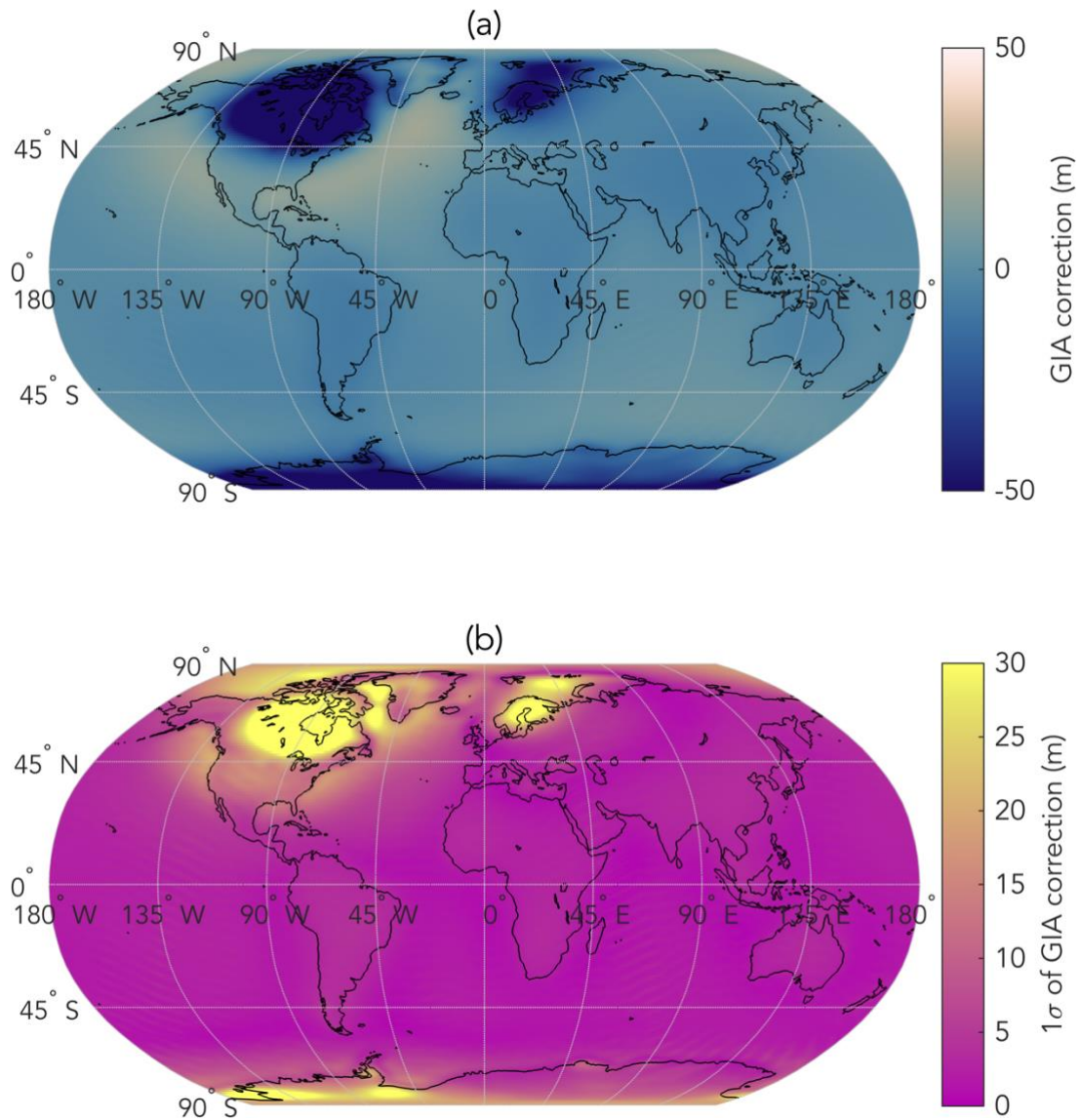
Figure 7: GIA correction and 1σ uncertainty associated with the assumed 1-D Earth structure based on Pleistocene-to-present disequilibrium computed by Raymo et al. (2011). (a): Mean GIA correction based on 36 radially symmetric viscosity structures. (b): One standard deviation (1σ) of the mean correction.

3.3 DT change correction

Our full suite of DT change predictions over the last 3 Myr yields highly variable spatial patterns of deformation across the globe with amplitudes of up to ~ ± 200 m (Fig. 8; Supplementary Fig. 2). This variability is due to uncertainties in the thermal and viscosity structure of the mantle as well as uncertainties in plate motions. As a result, no individual model prediction simultaneously matches the observed residual deformation after correcting for GIA at all scarp locations (Fig. 9), precluding

21

a unified inference of Pliocene GMSL from any one DT model. At five of the ten sites, subsets of the DT change suite meet the stringent MSWD (<20) and GMSL (10 m to 40 m) criteria: Kongo Central (DRC), Mahafaly (Madagascar), De Hoop (South Africa), Socotra (Yemen), and Nome (Alaska, USA; Fig. 9c,e,g,h,i). Just one model meets the stringent criteria at the Kongo Central site and predicts southward upward tilting in agreement with the observations (Fig. 9c). While this model falls within the range of data in the north, it begins to underpredict deformation in the south. At the Mahafaly (Madagascar) site, a greater subset of models (n = 8) meets the stringent criteria; all of these models predict uniform elevation change along the scarp within the range of the data (Fig. 9e). The subset of DT models that meets the stringent criteria at the De Hoop (South Africa) site (n = 3) predicts a subtle decrease (~5 m) in elevations from west to east, which is somewhat consistent with the data, which show mostly uniform elevations along the scarp's length (Fig. 9g). In Socotra (Yemen), one model fulfills the stringent criteria but fails to capture the short wavelength variability that occurs at ~30 km distance (Fig. 9h). The largest subset (n = 15) of models that meets the stringent criteria occurs at the Nome (Alaska, USA) site, but no model in this subset captures the stark increase in elevation at the easternmost point of the scarp (Fig. 9i).
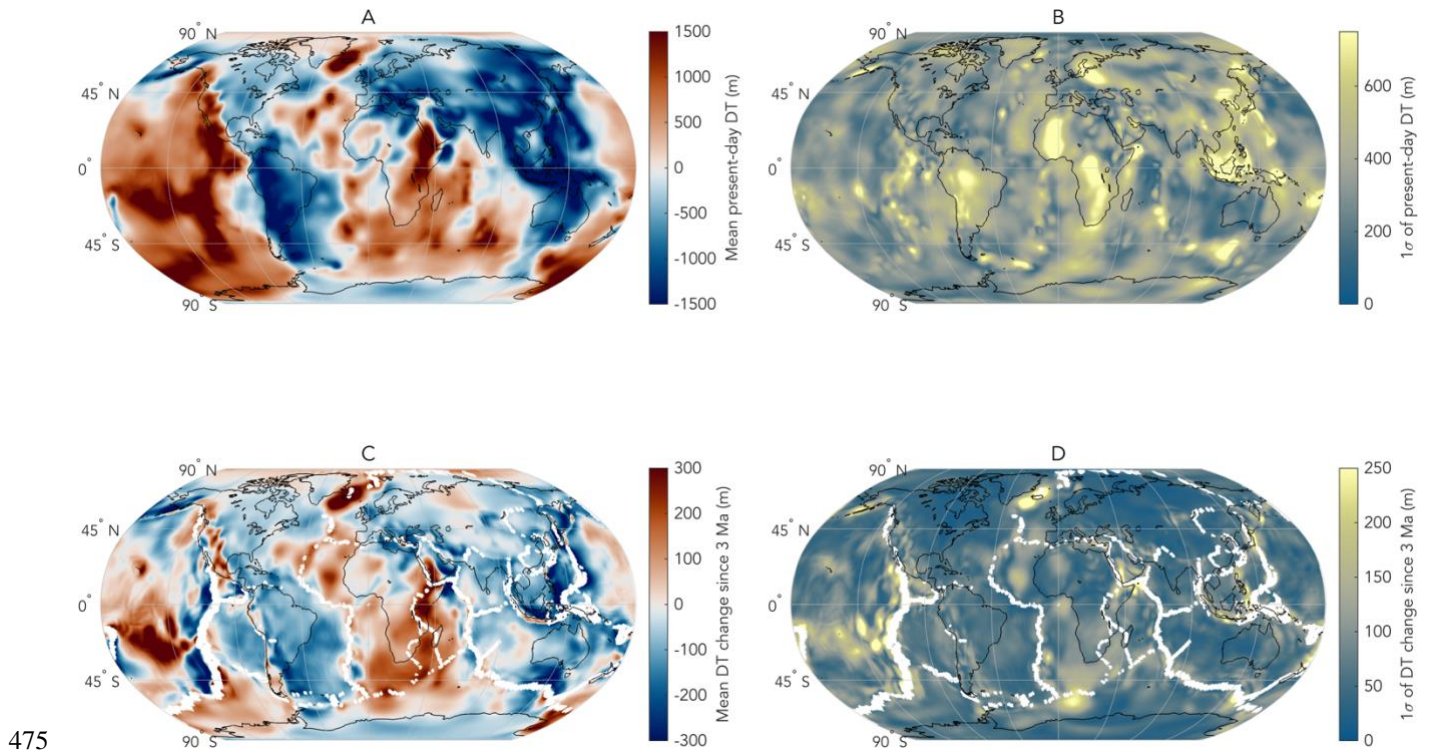

Figure 8: Present-day and change in DT over 3 Myrs model predictions. (a) Mean of present-day DT across convection suite (n = 27); (b) 1σ of the mean present-day DT prediction; (c) the mean of the change in DT over 3 Myrs across the convection suite (n = 135); (d) 1σ of the mean DT change over 3 Myrs with plate motion corrections applied.

At the Darling (Australia), Roe Plain (Australia), Benghazi (Libya), Al Wusta (Oman), and East Coast (USA) sites, no model achieves our stringent MSWD and GMSL criteria. When applying the weak criteria (MSWD <30 and GMSL between 0 m and 50 m), these sites coincide with small subsets of the DT change suite (excluding Benghazi, Libya, which

does not fit even the weak criteria). At the Darling (Australia) site, the subset (n = 3) that fulfills the weak criteria falls within the range of the observations in the south but fails to capture the assumed uplift (~40 m) in the north (Fig. 9a). At the Roe Plain (Australia) site, the weak criteria subset (n = 4) predicts linear patterns of deformation but not the anticlinal structure apparent in the observations (Fig. 9b). At the Al Wusta (Oman) site, the weak criteria model subset (n = 4) predicts first-order agreement with the data with slightly higher elevations (~10 m to 20 m) in the south that transition to lower elevations (~10 m) in the north (Fig. 9f). Finally, the East Coast (USA) scarp is consistent with a weak criteria model subset (n = 4) that predicts gradual uplift from ~0 m to ~40 m over ~600 km distance, which is consistent to first order with the spatial pattern of deformation but underpredicts the amplitude of change from the observations (Fig. 9j).

By applying this filtering criteria, we identify at each site which convection parameters are preferred (Fig. 9). A systematic preference for a radial reference viscosity and plate rotation correction is lacking; however, scarp locations appear sensitive to the specific upper mantle structure that is assigned in the model. The Darling (Australia), Roe Plain (Australia), and the East Coast (USA) sites, where only the weak fitting criteria were met by DT change predictions, all employ the upper mantle structure from the SL2013sv tomography model (Fig. 9a,b,j; Schaeffer & Lebedev, 2013). At the Mahafaly (Madagascar), Al Wusta (Oman), and Socotra (Yemen) sites, where models meet both the weak and stringent criteria, the best-fitting models are parameterized exclusively with upper mantle structure from the TX2008 model (Fig. 9e,f,h; Simmons et al., 2009). No site contains best-fitting models constrained exclusively by upper mantle structure from GLAD-M25; however, the best-fitting models for Kongo Central (DRC), De Hoop (South Africa), and Nome (Alaska, USA) consist of upper mantle structures from both GLAD-M25 and SL2013sv (Fig. 9c,g,i; Lei et al., 2020; Schaeffer & Lebedev, 2013).

(a) Darling (Australia)
(b) Roe Plain (Australia)
(c) Kongo Central (DRC) — GMSL = 13.2±10.1 m
(d) Benghazi (Libya)
(e) Mahafaly (Madagascar) — GMSL = 10.1±8.2 m
(f) Al Wusta (Oman)
(g) De Hoop (South Africa) — GMSL = 11.6±5.2 m
(h) Socotra (Yemen) — GMSL = 16.9±14.7 m
(i) Nome (Alaska, USA) — GMSL = 10.8±18.6 m
(j) East Coast (USA)
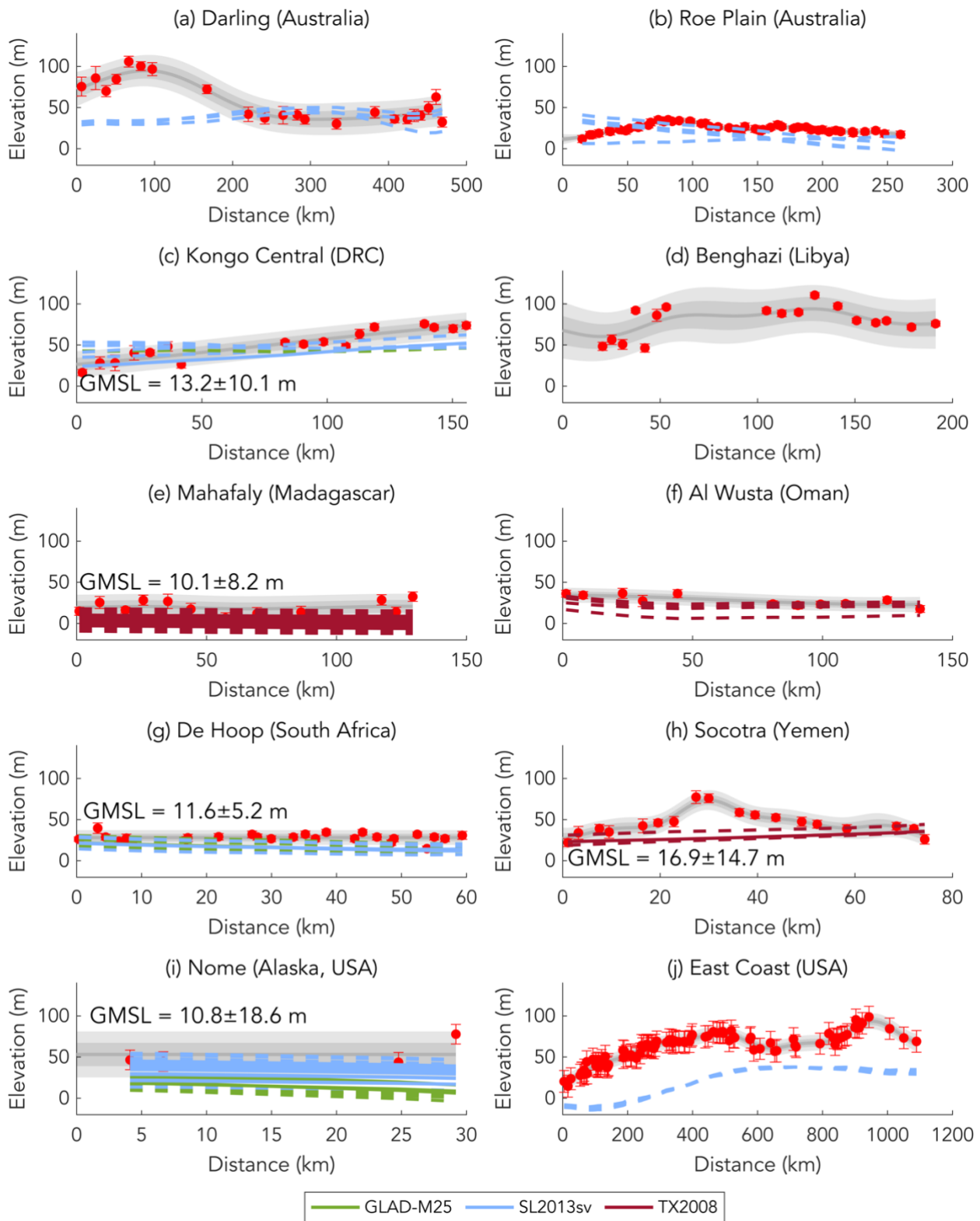
GLAD-M25   SL2013sv   TX2008

Figure 9: Comparison of GIA-corrected scarp deformation with predictions of DT change. Red points indicate mapped scarp elevations corrected for GIA. Their uncertainties are the square root of the sum of the squares of the individual uncertainties from the indicative range, field measurements, TerraceM analysis (Jara-Muñoz et al., 2016), and the GIA correction. Gray lines show Gaussian Process Regression models trained with the GIA-corrected elevation data. Dark and light gray bands correspond to 1σ and 2σ uncertainties of the Gaussian model, respectively. Green, blue, and red lines show predictions of DT change with upper mantle structures from the GLAD-M25, SL2013sv, and TX2008 tomography models, respectively (Lei et al., 2020; Schaeffer & Lebedev, 2013; Simmons et al., 2009). Solid colored lines correspond to DT change solutions that fit the stringent fitting criteria. Dashed colored lines correspond to DT change solutions that meet the weak fitting criteria. The inferred GMSL and fully propagated uncertainty is shown for sites that meet the stringent fitting criteria. (a) Darling (Australia); (b) Roe Plain (Australia); (c) Kongo Central (DRC); (d) Benghazi (Libya); (e) Mahafaly (Madagascar); (f) Al Wusta (Oman); (g) De Hoop (South Africa); (h) Socotra (Yemen); (i) Nome (Alaska, USA); (j) East Coast (USA).

4 Discussion

With the dual motivation of (1) improving the accuracy of mantle convection simulations and (2) using predictions of mantle DT change to correct for solid Earth deformation to infer Pliocene GMSL, we present a dataset of ten globally distributed scarps that record ancient sea-level highstands. Data-model comparison demonstrates that our current generation of convection models is incapable of accurately simulating deformation at each site simultaneously, and in the following sections we explore several reasons for data-model misfit and recommendations for future work.

4.1 Data-model misfit due to data uncertainties

While this dataset is a result of rigorous analysis of each scarp's geomorphology, in which we use high-resolution DEMs, direct field mapping, and secondary analysis of landscape evolution, a considerable amount of subjectivity can be involved in interpreting sometimes complex geologic archives of past sea level. For example, while many coast-perpendicular topography profiles are characterized by easily-identified platform and cliff geometries (e.g., the Al Wusta (Oman) and Roe Plain (Australia) sites), many others are not (e.g., the Mahafaly (Madagascar) site) and involve uncertain choices about defining scarp structure. One important cause of uncertainty is the presence of dunes on the coastal plain, which if not identified properly, can lead to an overestimate of the platform elevation. Field mapping reduces the subjectivity involved in analyzing DEMs; however, many of the scarps included here were not mapped through direct observations. In some cases (e.g., the Benghazi (Libya) site), a cliff is well defined in cross section, but the platform appears mostly buried by surface sediments, obfuscating its structure (Fig. 4d). At other locations, such as the Kongo Central (DRC) site, the platform is well defined but shows high-frequency variability in cross section that increases uncertainties in the extrapolated intersection (i.e., scarp toe; Fig. 4c).

In addition to challenges associated with characterizing the structure of the scarps, age uncertainties play a vital role in the comparison between scarp elevation data and geodynamic predictions. All of the convection simulations that we present correspond to DT change over the last 3 Myr, which approximately corresponds to deformation since the MPWP. That said, the true formation age of the scarps may be challenging to discern without an absolute geochronology. As predicted by the Trenhaile (2014) model framework, high frequency, orbitally paced sea-level oscillations would have carved away steep cliff

25

faces and deposited horizontal coastal plains. However, these sea-level highstands may not have affected every site equally, owing to geographically variable sea-level change and geodynamic conditions. To preserve the sea-level marker, this formational model depends on a background geodynamic state where the crust undergoes either no uplift or slow rates of
540 uplift; subsiding regions may cause erosion platforms to be submerged and ultimately not preserved in the topography. At sites where data-model misfit is great (e.g., the Benghazi (Libya) site), the age uncertainty may in part explain the misfit; however, the misfit does not provide decisive information about whether the true age of the scarp is younger or older than the simulation. On the other hand, a low data-model misfit may indicate a scarp's formation age is indeed close to 3 Ma (e.g., the De Hoop (South Africa), Kongo Central (DRC), and Al Wusta (Oman) sites).

545 **4.2 Data-model misfit due to model uncertainties and proposed improvements**

After correcting each scarp for GIA, a process that alone cannot explain all of the observed deformation, we compare the residual deformation with predictions of DT change. Despite the success of some predictions of DT change, nearly all sites within this dataset are characterized by shorter wavelength elevation variability than is simulated by our models (Fig. 9). This is most apparent at the Socotra (Yemen) scarp, where the scarp's elevations reflect an anticlinal geometry over <80 km distance
550 (Fig. 9h) that is not seen in the DT model predictions. Slightly longer wavelength (150 km to 500 km) anticlinal structures are also apparent at the Darling (Australia), Roe Plain (Australia), and East Coast (USA) sites, and our preferred models at those locations yield only moderate success at reproducing this short-wavelength variability (Fig. 9a,b,j). Importantly, the wavelength of DT is directly related to the wavelength of the particular upper mantle tomography model used in our convection simulations; SL2013sv consists of the shortest wavelength mantle structure that is included in our convection suite and
555 performs well for most sites in the dataset.

By generating a large suite of convection simulations, we are able to assess which localities favor certain model parameters. We find that the upper mantle buoyancy structure has a first-order impact on the success of our models at any given location (Fig. 3; Fig. 10). For example, only models constrained by the TX2008 tomography model produce realistic predictions of along-scarp deformation and inferred GMSL at the Mahafaly (Madagascar), Al Wusta (Oman), and Socotra
560 (Yemen) scarps (Fig. 9e,f,h; Fig. 10). These locations are all in the proximity of the African superplume (Ni et al., 2002; Simmons et al., 2007). The TX2008 model is the only one in our suite in which density perturbations were tuned to fit present-day surface observations (e.g., the global free-air gravity field, tectonic plate divergences, and DT). This model employs laterally varying correction factors to the shear wave velocity-to-density scaling, a procedure that constrains important compositional variation between mantle plume structures (as well as cratonic roots) and the ambient mantle. Our simulations
565 constrained by SL2013sv and GLAD-M25-derived upper mantle structure are not well suited for these sites, as our conversion from seismic velocity-to-temperature neglects the compositional difference of superplumes from the surrounding mantle; this leads to upwelling above plume structures in these models that are too fast (Fig. 10). That said, many other sites, including the Darling (Australia), Roe Plain (Australia), Kongo Central (DRC), and East Coast (USA) scarps are only compatible with

26

models parameterized with SL2013sv-derived upper mantle structure (Fig. 9a,b,c,j; Fig. 10). This model is the only one that

570 also uses surface waves in the inversion, which resolves shorter wavelength upper mantle structure that appears to be important

to predict DT change along these passive margins. Our models capture the ability of short-wavelength lithospheric structure

to promote small-scale convection and DT variations but are limited by the spatial resolution of tomography models.
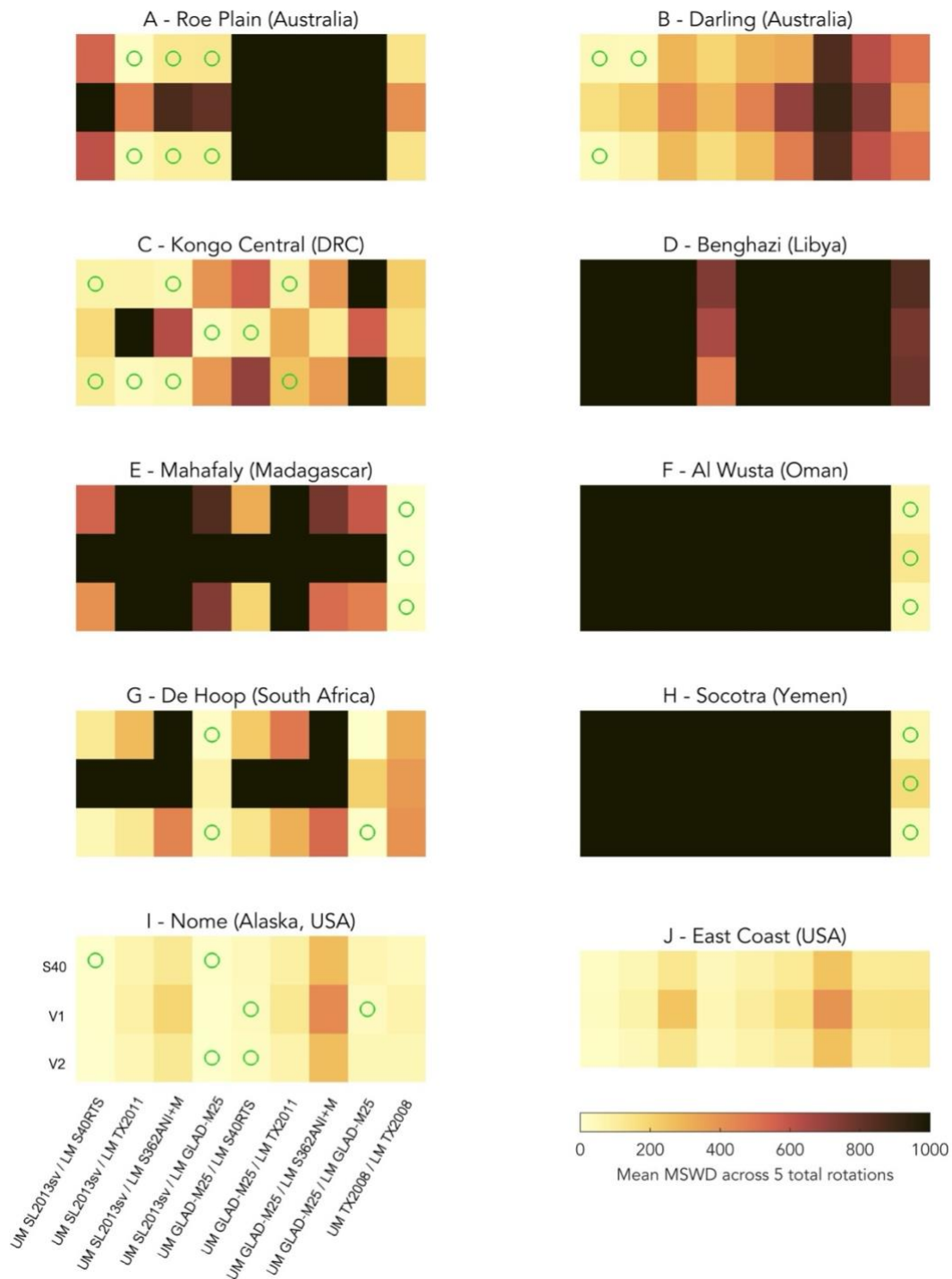
Figure 10: Heatmaps of convection suite parameter space and mean MSWD across the five total rotations. Green circles indicate viscosity-Earth model pairs where at least one total rotation correction leads to a GMSL inference that falls within the range of 10 m to 40 m. (a) Roe Plain (Australia); (b) Darling (Australia); (c) Kongo Central (DRC); (d) Benghazi (Libya); (e)

28

Mahafaly (Madagascar); (f) Al Wusta (Oman); (g) De Hoop (South Africa); (h) Socotra (Yemen); (i) Nome (Alaska, USA); (j) East Coast (USA).

580   Our data-model comparison provides insight into how models can be improved. As the present-day 3-D buoyancy structure has a first-order influence over the convective regime, improving this constraint by incorporating regional tomography models or those that employ surface waves will be critical. The calibrated parameterization of the Yamauchi & Takei (2016) shear wave velocity-to-temperature conversion by Richards et al. (2020) provides a necessary constraint on the effects of anelasticity on seismic velocity and ultimately on the inferred properties of the mantle. However, improvements to

585   this conversion that invoke new data constraints can serve to better predict mantle temperatures, densities, and viscosities. In addition, accurate parameterization of compositional structures (e.g., lithosphere and Large Low-Shear-Velocity Provinces) will have important effects on DT predictions (Richards, Hoggard, et al., 2023). While our models incorporate lateral viscosity variations, they likely underestimate the true amplitude of variability (Yang & Gurnis, 2016), and while increasing this contrast comes with computational expense, it remains a worthwhile objective. Compressibility, phase transitions, and non-linear

590   rheology are some further improvements that invoke more complex physics and will improve the fidelity of DT results as well (Colli et al., 2018; Tackley, 2008). Lastly, we highlight that geodynamic inverse frameworks, in particular the adjoint approach (e.g., Ghelichkhan et al., 2021), may be uniquely positioned to invert for viscosity and density structures in the mantle that produce the observed topographic change.

4.3 Data-model misfit due to potential auxiliary deformation processes

595   In addition to data and model deficiencies, auxiliary processes, which include flexure and isostatic adjustment due to sedimentary load changes (e.g., Moucha & Ruetenik, 2017) or brittle deformation in the crust (i.e., faulting), are potential sources of short-wavelength variability in the topography. These auxiliary processes are not explicitly accounted for in our modeling framework. For example, the Socotra (Yemen) and Benghazi (Libya) scarps occur peripheral to active tectonic boundaries, and while compelling evidence of crustal deformation would require better field observations, these sites have

600   likely been deformed at least in part by tectonic processes. This factor may also be related to their higher mapped elevations in comparison to other sites in the dataset (Fig. 5 & 8). While the Darling (Australia) site also falls within this higher elevation range (maximum elevation >100 m) and is situated near-parallel to the prominent Darling Fault (Fig. 3a), it is not likely that crustal processes deformed the scarp since the Darling Fault was last active during times much earlier than is relevant to the formation of the scarp (Fletcher et al., 1985). Other sites, such as the East Coast (USA), exhibit considerable residual

605   deformation after both the GIA and DT change corrections have been applied. This is likely a result of sedimentary loading and crustal flexure, which are not accounted for in our modeling framework but are thought to be important processes for this region (Moucha & Ruetenik, 2017). The Al Wusta (Oman) site is located peripheral to salt diapirism, a regional process that occurs on million year-timescales and may be relevant to the site's recent deformation (Li et al., 2012). Diffusive landscape evolution at most sites also contributes to the observed topography, but we attempt to correct for this through our TerraceM

analysis (Fig. 4). All of these effects occur synchronously with DT change and must be considered to unravel the full deformational history of any site, emphasizing the need to consider regional processes.

4.4 GMSL inference and implications

While data and model uncertainties persist, there are five scarps for which along-scarp deformation and the magnitude of deformation in the models are consistent (Fig. 9; solid lines): Kongo Central (DRC), Mahafaly (Madagascar), De Hoop (South Africa), Socotra (Yemen), and Nome (Alaska, USA). We calculate the inferred GMSL for each site using the DT prediction that yields the best fit (lowest MSWD) to the along-scarp deformation. These locations show minimal residual deformation after all corrections have been applied, suggesting that auxiliary processes may not have played a major role in their deformation since 3 Ma. These five sites produce GMSL estimates of 13.1 ± 10.1 m (Kongo Central, DRC), 10.1 ± 8.2 m (Mahafaly, Madagascar), 11.6 ± 5.2 m (De Hoop, South Africa), 16.9 ± 14.7 m (Socotra, Yemen), and 10.8 ± 18.6 m (Nome, Alaska, USA; Fig 8c,e,g,h,i). The De Hoop (South Africa) site in particular has comparatively good age control (3.56 ± 1.08 Ma; Rovere et al., 2014) and the lowest GMSL uncertainty, which makes this our most reliable constraint. The preferred model also predicts patterns of present-day DT consistent with observations (present-day DT varying from ~100 m to >500 m; Hoggard et al., 2017). The remaining four sites are characterized by greater GMSL uncertainty and misfit with residual topography observations.

The De Hoop (South Africa) mean estimate for MPWP GMSL is lower than the inference from Mallorca (16.2 m; 3.27 ± 0.12 Ma) but falls within the reported 1σ uncertainty (5.6 m to 19.2 m; Dumitru et al., 2019). If valid, this lower range may suggest ice sheets were relatively stable even under warm Pliocene climate conditions (2.5˚C to 4˚C above 1850 to 1900 baseline; Fedorov et al., 2013; Fischer et al., 2018; Haywood et al., 2013). With the Greenland Ice Sheet contributing ~7 m (Bierman et al., 2016; Morlighem et al., 2017), the West Antarctic Ice Sheet contributing ~3.2 m from its most unstable sectors (Bamber et al., 2009), and thermal expansion contributing ~1.5 m (Dumitru et al., 2019), little to no excess melt contribution from the East Antarctic Ice Sheet is required to fit this Pliocene sea-level budget.

5 Conclusion

We present a dataset of ten wavecut scarps that formed during Pliocene times, when Earth's mean temperatures were similar to and higher than present-day levels. This interval is a critical target for sea-level reconstructions because it can be used to calibrate projections of sea-level rise this century (e.g., DeConto et al., 2021). We use a combination of high-resolution remote sensing, direct field mapping, and landscape evolution analysis (i.e., TerraceM) to characterize the topography of each scarp. These globally distributed sites show patterns of short-wavelength variability in the topography, which has resulted from ~3 Myr of solid Earth deformation primarily due to GIA and DT change as well as brittle deformation in the crust, flexure due to sedimentary load changes, and surface deposition or incision. As deformation due to GIA is characterized by significantly lower amplitude and uncertainty, especially in the far field of Pleistocene ice sheets, DT change represents a much more

uncertain correction owing to the many under-constrained parameters involved in simulating mantle convection. We compare a large suite of DT change predictions (n = 135) to the scarp dataset and find that no individual DT change model can accurately predict epeirogenic motion at every site; however, model fits exist for selected sites. This data-model comparison informs proposed model improvements, largely focused on better constraining upper mantle structure and rheology. Despite persistent uncertainties in both the data and models, we use our best-fitting predictions to remove the effects due to GIA and DT change and compute GMSL estimates. Our preferred GMSL inference (11.6 ± 5.2 m) from the De Hoop (South Africa) site falls in the lower range of existing estimates for the MPWP. If valid, this would suggest ice sheets may have been more resistant to the warm Pliocene climate conditions than previously thought. Nonetheless, Pliocene results confirm that Earth's present-day ice sheets are increasingly out of equilibrium with heat and greenhouse gas in the atmosphere, likely leading to multi-meter sea-level rise in the coming centuries.

Author contribution

MR, AR, AH, and JA conceptualized the project. MR, JA, and AR were responsible for funding acquisition. AH performed the scarp analysis with input from AR and JA. AH implemented the GIA corrections with input from JA. AH performed the

mantle convection simulations with input from JA, FR, and MH. All authors contributed to investigation as well as writing and editing the manuscript.

Data availability

We have made the mantle convection code, ASPECT (version 2.2.0), available on Github

675 (https://github.com/ahollyday/aspect/tree/g_cubed_2022; Bangerth, Dannberg, Gassmoeller, & Heister, 2020). The necessary inputs, including initial temperature, viscosity, LAB extent files, and an example parameter file for models run by Hollyday et al. (2023), are archived at DOI 10.5281/zenodo.7508207. We have made the three additional initial temperature models from this study available at DOI (*will be generated upon article acceptance*).

References

680 Abbasi, I. A., Hersi, O. S., Al-Harthy, A., & Al-Rashdi, I. (2013). Lithofacies attributes, depositional system and diagenetic properties of the Permian Gharif Formation from Haushi–Huqf area, Central Oman. *Arabian Journal of Geosciences*, *6*(12), 4931–4945. https://doi.org/10.1007/s12517-012-0763-7

Argus, D. F., Gordon, R. G., & DeMets, C. (2011). Geologically current motion of 56 plates relative to the no-net-rotation reference frame. *Geochemistry, Geophysics, Geosystems*, *12*(11). https://doi.org/10.1029/2011GC003751

685 Austermann, J., & Mitrovica, J. X. (2015). Calculating gravitationally self-consistent sea level changes driven by dynamic topography. *Geophysical Journal International*, *203*(3), 1909–1922. https://doi.org/10.1093/gji/ggv371

Austermann, J., Mitrovica, J. X., Huybers, P., & Rovere, A. (2017). Detection of a dynamic topography signal in last interglacial sea-level records. *Science Advances*, *3*(7), e1700457. https://doi.org/10.1126/sciadv.1700457

Austermann, J., Pollard, D., Mitrovica, J. X., Moucha, R., Forte, A. M., DeConto, R. M., Rowley, D. B., & Raymo, M. E.
690 (2015). The impact of dynamic topography change on Antarctic ice sheet stability during the mid-Pliocene warm period. *Geology*, *43*(10), 927–930. https://doi.org/10.1130/G36988.1

Bamber, J. L., Riva, R. E. M., Vermeersen, B. L. A., & LeBrocq, A. M. (2009). Reassessment of the Potential Sea-Level Rise from a Collapse of the West Antarctic Ice Sheet. *Science*, *324*(5929), 901–903. https://doi.org/10.1126/science.1169335

695 Bangerth, W., Dannberg, J., Gassmoeller, R., Heister, T., & others. (2020). *ASPECT: Advanced Solver for Problems in Earth's ConvecTion, User Manual*. https://doi.org/10.6084/m9.figshare.4865333.v7

Beydoun, Z. R., & Bichan, H. R. (1969). The geology of Socotra Island, Gulf of Aden. *Quarterly Journal of the Geological Society*, *125*(1–4), 413–441. https://doi.org/10.1144/gsjgs.125.1.0413

Bierman, P. R., Shakun, J. D., Corbett, L. B., Zimmerman, S. R., & Rood, D. H. (2016). A persistent and dynamic East

700   Greenland Ice Sheet over the past 7.5 million years. *Nature*, *540*(7632), Article 7632.
https://doi.org/10.1038/nature20147

Birse, A. C. R., Bott, W. F., Morrison, J., & Samuel, M. A. (1997). The Mesozoic and early tertiary tectonic evolution of the Socotra area, eastern Gulf of Aden, Yemen. *Marine and Petroleum Geology*, *14*(6), 675–684. https://doi.org/10.1016/S0264-8172(96)00043-8

705   Burke, K. D., Williams, J. W., Chandler, M. A., Haywood, A. M., Lunt, D. J., & Otto-Bliesner, B. L. (2018). Pliocene and Eocene provide best analogs for near-future climates. *Proceedings of the National Academy of Sciences*, *115*(52), 13288–13293. https://doi.org/10.1073/pnas.1809600115

Colli, L., Ghelichkhan, S., Bunge, H.-P., & Oeser, J. (2018). Retrodictions of Mid Paleogene mantle flow and dynamic topography in the Atlantic region from compressible high resolution adjoint mantle convection models: Sensitivity

710   to deep mantle viscosity and tomographic input model. *Gondwana Research*, *53*, 252–272. https://doi.org/10.1016/j.gr.2017.04.027

Czarnota, K., Hoggard, M. J., White, N., & Winterbourne, J. (2013). Spatial and temporal patterns of Cenozoic dynamic topography around Australia. *Geochemistry, Geophysics, Geosystems*, *14*(3), 634–658. https://doi.org/10.1029/2012GC004392

715   Dandouau, A. (1922). *Géographie de Madagascar.* Larose.

Davis, W. M. (1933). Glacial Epochs of the Santa Monica Mountains, California. *GSA Bulletin*, *44*(5), 1041–1133. https://doi.org/10.1130/GSAB-44-1041

DeConto, R. M., Pollard, D., Alley, R. B., Velicogna, I., Gasson, E., Gomez, N., Sadai, S., Condron, A., Gilford, D. M., Ashe, E. L., Kopp, R. E., Li, D., & Dutton, A. (2021). The Paris Climate Agreement and future sea-level rise from

720   Antarctica. *Nature*, *593*(7857), Article 7857. https://doi.org/10.1038/s41586-021-03427-0

Dowsett, H. J., & Cronin, T. M. (1990). High eustatic sea level during the middle Pliocene:Evidence from the southeastern U.S. Atlantic Coastal Plain. *Geology*, *18*(5), 435–438. https://doi.org/10.1130/0091-7613(1990)018<0435:HESLDT>2.3.CO;2

Dumitru, O. A., Austermann, J., Polyak, V. J., Fornós, J. J., Asmerom, Y., Ginés, J., Ginés, A., & Onac, B. P. (2019).

725   Constraints on global mean sea level during Pliocene warmth. *Nature*, *574*(7777), Article 7777. https://doi.org/10.1038/s41586-019-1543-2

Edwards, T. L., Brandon, M. A., Durand, G., Edwards, N. R., Golledge, N. R., Holden, P. B., Nias, I. J., Payne, A. J., Ritz, C., & Wernecke, A. (2019). Revisiting Antarctic ice loss due to marine ice-cliff instability. *Nature*, *566*(7742), Article 7742. https://doi.org/10.1038/s41586-019-0901-4

730   Eisma, D., & Van Bennekom, A. J. (1978). The Zaire river and estuary and the Zaire outflow in the Atlantic ocean. *Netherlands Journal of Sea Research*, *3–4*. https://www.vliz.be/nl/imis?module=ref&refid=14113

Farr, T. G., Rosen, P. A., Caro, E., Crippen, R., Duren, R., Hensley, S., Kobrick, M., Paller, M., Rodriguez, E., Roth, L.,

Seal, D., Shaffer, S., Shimada, J., Umland, J., Werner, M., Oskin, M., Burbank, D., & Alsdorf, D. (2007). The Shuttle Radar Topography Mission. *Reviews of Geophysics*, *45*(2). https://doi.org/10.1029/2005RG000183

735   Farrell, W. E., & Clark, J. A. (1976). On Postglacial Sea Level. *Geophysical Journal International*, *46*(3), 647–667. https://doi.org/10.1111/j.1365-246X.1976.tb01252.x

Fedorov, A. V., Brierley, C. M., Lawrence, K. T., Liu, Z., Dekens, P. S., & Ravelo, A. C. (2013). Patterns and mechanisms of early Pliocene warmth. *Nature*, *496*(7443), Article 7443. https://doi.org/10.1038/nature12003

Fiduk, J. C. (2009). Evaporites, petroleum exploration, and the Cenozoic evolution of the Libyan shelf margin, central North

740   Africa. *Marine and Petroleum Geology*, *26*(8), 1513–1527. https://doi.org/10.1016/j.marpetgeo.2009.04.006

Fischer, H., Meissner, K. J., Mix, A. C., Abram, N. J., Austermann, J., Brovkin, V., Capron, E., Colombaroli, D., Daniau, A.-L., Dyez, K. A., Felis, T., Finkelstein, S. A., Jaccard, S. L., McClymont, E. L., Rovere, A., Sutter, J., Wolff, E. W., Affolter, S., Bakker, P., … Zhou, L. (2018). Palaeoclimate constraints on the impact of 2 °C anthropogenic warming and beyond. *Nature Geoscience*, *11*(7), Article 7. https://doi.org/10.1038/s41561-018-0146-0

745   Flament, N., Gurnis, M., & Müller, R. D. (2013). A review of observations and models of dynamic topography. *Lithosphere*, *5*(2), 189–210. https://doi.org/10.1130/L245.1

Fletcher, I. R., Wilde, S. A., & Rosman, K. J. R. (1985). Sm-Nd model ages across the margins of the Archaean Yilgarn Block, Western Australia—III. The western margin. *Australian Journal of Earth Sciences*, *32*(1), 73–82. https://doi.org/10.1080/08120098508729314

750   Fournier, M., Bellahsen, N., Fabbri, O., & Gunnell, Y. (2004). Oblique rifting and segmentation of the NE Gulf of Aden passive margin. *Geochemistry, Geophysics, Geosystems*, *5*(11). https://doi.org/10.1029/2004GC000731

Fournier, M., Chamot-Rooke, N., Petit, C., Huchon, P., Al-Kathiri, A., Audin, L., Beslier, M.-O., d'Acremont, E., Fabbri, O., Fleury, J.-M., Khanbari, K., Lepvrier, C., Leroy, S., Maillot, B., & Merkouriev, S. (2010). Arabia-Somalia plate kinematics, evolution of the Aden-Owen-Carlsberg triple junction, and opening of the Gulf of Aden. *Journal of*

755   *Geophysical Research: Solid Earth*, *115*(B4). https://doi.org/10.1029/2008JB006257

Fournier, M., Patriat, P., & Leroy, S. (2001). Reappraisal of the Arabia–India–Somalia triple junction kinematics. *Earth and Planetary Science Letters*, *189*(3), 103–114. https://doi.org/10.1016/S0012-821X(01)00371-5

GEBCO Compilation Group. (2023). *GEBCO 2023 Grid* [dataset]. https://doi.org/10.5285/f98b053b-0cbc-6c23-e053-6c86abc0af7b

760   Ghelichkhan, S., Bunge, H.-P., & Oeser, J. (2021). Global mantle flow retrodictions for the early Cenozoic using an adjoint method: Evolving dynamic topographies, deep mantle structures, flow trajectories and sublithospheric stresses. *Geophysical Journal International*, *226*(2), 1432–1460. https://doi.org/10.1093/gji/ggab108

Glišović, P., & Forte, A. M. (2015). Importance of initial buoyancy field on evolution of mantle thermal structure: Implications of surface boundary conditions. *Geoscience Frontiers*, *6*(1), 3–22.

765   https://doi.org/10.1016/j.gsf.2014.05.004

Grand, S. P. (2002). Mantle shear–wave tomography and the fate of subducted slabs. *Philosophical Transactions of the*

34

Royal Society of London. Series A: Mathematical, Physical and Engineering Sciences, *360*(1800), 2475–2491. https://doi.org/10.1098/rsta.2002.1077

Grant, G. R., Naish, T. R., Dunbar, G. B., Stocchi, P., Kominz, M. A., Kamp, P. J. J., Tapia, C. A., McKay, R. M., Levy, R. H., & Patterson, M. O. (2019). The amplitude and origin of sea-level variability during the Pliocene epoch. *Nature*, *574*(7777), Article 7777. https://doi.org/10.1038/s41586-019-1619-z

Grant, K. M., Rohling, E. J., Ramsey, C. B., Cheng, H., Edwards, R. L., Florindo, F., Heslop, D., Marra, F., Roberts, A. P., Tamisiea, M. E., & Williams, F. (2014). Sea-level variability over five glacial cycles. *Nature Communications*, *5*(1), Article 1. https://doi.org/10.1038/ncomms6076

Graybill, E. A., Harris, P. T., Kelley, P., & Dietl, D. P. (2009). *Age of the Duplin and Waccamaw Formations, Cape Fear River Basin, North Carolina*. GSA Southeastern Section - 58th Annual Meeting. https://www.researchgate.net/publication/256843578_Age_of_the_Duplin_and_Waccamaw_Formations_Cape_Fear_River_Basin_North_Carolina

Grosjean, E., Love, G. D., Stalvies, C., Fike, D. A., & Summons, R. E. (2009). Origin of petroleum in the Neoproterozoic –Cambrian South Oman Salt Basin. *Organic Geochemistry*, *40*(1), 87–110. https://doi.org/10.1016/j.orggeochem.2008.09.011

Guiraud, M., Buta-Neto, A., & Quesne, D. (2010). Segmentation and differential post-rift uplift at the Angola margin as recorded by the transform-rifted Benguela and oblique-to-orthogonal-rifted Kwanza basins. *Marine and Petroleum Geology*, *27*(5), 1040–1068. https://doi.org/10.1016/j.marpetgeo.2010.01.017

Hallett, D. (2002). *Petroleum Geology of Libya—2nd Edition*. https://www.elsevier.com/books/petroleum-geology-of-libya/hallett/978-0-444-63517-4

Hanna, S. S. (1990). The Alpine deformation of the Central Oman Mountains. *Geological Society, London, Special Publications*, *49*(1), 341–359. https://doi.org/10.1144/GSL.SP.1992.049.01.21

Haywood, A. M., Hill, D. J., Dolan, A. M., Otto-Bliesner, B. L., Bragg, F., Chan, W.-L., Chandler, M. A., Contoux, C.,Dowsett, H. J., Jost, A., Kamae, Y., Lohmann, G., Lunt, D. J., Abe-Ouchi, A., Pickering, S. J., Ramstein, G., Rosenbloom, N. A., Salzmann, U., Sohl, L., … Zhang, Z. (2013). Large-scale features of Pliocene climate: Results from the Pliocene Model Intercomparison Project. *Climate of the Past*, *9*(1), 191–209. https://doi.org/10.5194/cp-9-191-2013

Hearty, P. J., Rovere, A., Sandstrom, M. R., O'Leary, M. J., Roberts, D., & Raymo, M. E. (2020). Pliocene-Pleistocene Stratigraphy and Sea-Level Estimates, Republic of South Africa With Implications for a 400 ppmv CO2 World. *Paleoceanography and Paleoclimatology*, *35*(7), e2019PA003835. https://doi.org/10.1029/2019PA003835

Heister, T., Dannberg, J., Gassmöller, R., & Bangerth, W. (2017). High accuracy mantle convection simulation through modern numerical methods – II: Realistic models and problems. *Geophysical Journal International*, *210*(2), 833–851. https://doi.org/10.1093/gji/ggx195

Hoggard, M. J., White, N., & Al-attar, D. (2016). Global dynamic topography observations reveal limited influence of large

-scale mantle flow. *Nature Geoscience; London*, *9*(6), 456–463.

http://dx.doi.org.ezproxy.cul.columbia.edu/10.1038/ngeo2709

Hoggard, M. J., Winterbourne, J., Czarnota, K., & White, N. (2017). Oceanic residual depth measurements, the plate cooling model, and global dynamic topography. *Journal of Geophysical Research: Solid Earth*, *122*(3), 2328–2372.

805   https://doi.org/10.1002/2016JB013457

Hollyday, A., Austermann, J., Lloyd, A., Hoggard, M., Richards, F., & Rovere, A. (2023). A Revised Estimate of Early Pliocene Global Mean Sea Level Using Geodynamic Models of the Patagonian Slab Window. *Geochemistry, Geophysics, Geosystems*, *24*(2), e2022GC010648. https://doi.org/10.1029/2022GC010648

Huddlestun, P. F. (1988). *A revision of the lithostratigraphic units of the coastal plain of Georgia: The Miocene through*

810   *Holocene*. Environmental Protection Division, Georgia Department of Natural Resources.

James, N. P., & Bone, Y. (2007). A LATE PLIOCENE–EARLY PLEISTOCENE, INNER-SHELF, SUBTROPICAL, SEAGRASS-DOMINATED CARBONATE: ROE CALCARENITE, GREAT AUSTRALIAN BIGHT, WESTERN AUSTRALIA. *PALAIOS*, *22*(4), 343–359. https://doi.org/10.2110/palo.2005.p05-117r

James, N. P., Bone, Y., Carter, R. M., & Murray-Wallace, C. V. (2006). Origin of the Late Neogene Roe Plains and their

815   calcarenite veneer: Implications for sedimentology and tectonics in the Great Australian Bight. *Australian Journal of Earth Sciences*, *53*(3), 407–419. https://doi.org/10.1080/08120090500499289

Jara-Muñoz, J., Melnick, D., & Strecker, M. R. (2016). TerraceM: A MATLAB® tool to analyze marine and lacustrine terraces using high-resolution topography. *Geosphere*, *12*(1), 176–195. https://doi.org/10.1130/GES01208.1

Jordan, T. H. (1978). Composition and development of the continental tectosphere. *Nature*, *274*(5671), Article 5671.

820   https://doi.org/10.1038/274544a0

Kaufman, D. S., & Brigham-Grette, J. (1993). Aminostratigraphic correlations and paleotemperature implications, Pliocene -Pleistocene high-sea-level deposits, northwestern Alaska. *Quaternary Science Reviews*, *12*(1), 21–33. https://doi.org/10.1016/0277-3791(93)90046-O

Kelsey, H. M. (2015). Geomorphological indicators of past sea levels. In *Handbook of Sea-Level Research* (pp. 66–82). John

825   Wiley & Sons, Ltd. https://doi.org/10.1002/9781118452547.ch5

Kendrick, G. W., Wyrwoll, K.-H., & Szabo, B. J. (1991). Pliocene-Pleistocene coastal events and history along the western margin of Australia. *Quaternary Science Reviews*, *10*(5), 419–439. https://doi.org/10.1016/0277-3791(91)90005-F

Kronbichler, M., Heister, T., & Bangerth, W. (2012). High accuracy mantle convection simulation through modern numerical methods. *Geophysical Journal International*, *191*(1), 12–29. https://doi.org/10.1111/j.1365-

830   246X.2012.05609.x

Kumar, A. (2015). Geological and environmental features around Brega region, Libya. *Earth Science India (Popular Issue)*, *VIII*, 1–14.

Lei, W., Ruan, Y., Bozdağ, E., Peter, D., Lefebvre, M., Komatitsch, D., Tromp, J., Hill, J., Podhorszki, N., & Pugmire, D.

(2020). Global adjoint tomography—Model GLAD-M25. *Geophysical Journal International*, *223*(1), 1–21.
https://doi.org/10.1093/gji/ggaa253

Li, S., Abe, S., Reuning, L., Becker, S., Urai, J. L., & Kukla, P. A. (2012). Numerical modelling of the displacement and deformation of embedded rock bodies during salt tectonics: A case study from the South Oman Salt Basin. *Geological Society, London, Special Publications*, *363*(1), 503–520. https://doi.org/10.1144/SP363.24

Lisiecki, L. E., & Raymo, M. E. (2005). A Pliocene-Pleistocene stack of 57 globally distributed benthic δ18O records. *Paleoceanography*, *20*(1). https://doi.org/10.1029/2004PA001071

Lorscheid, T., & Rovere, A. (2019). The indicative meaning calculator – quantification of paleo sea-level relationships by using global wave and tide datasets. *Open Geospatial Data, Software and Standards*, *4*(1), 10. https://doi.org/10.1186/s40965-019-0069-8

Malan, J. A. (1991). *Lithostratigraphy of the De Hoopvlei Formation (Bredasdorp Group) / J.A. Malan ; South African Committee for Stratigraphy. - Vanderbilt University*. https://catalog.library.vanderbilt.edu/discovery/fulldisplay/alma991019959639703276/01VAN_INST:vanui

Masson-Delmotte, V., Zhai, P., Pirani, A., Connors, S. L., Péan, C., Berger, S., Caud, N., Chen, Y., Goldfarb, L., Gomis, M. I., Huang, M., Leitzell, K., Lonnoy, E., Matthews, J. B. R., Maycock, T. K., Waterfield, T., Yelekçi, O., Yu, R., & Zhou, B. (2021). *Climate Change 2021: The Physical Science Basis. Contribution of Working Group 1 to the Sixth Assessment Report of the International Panel on Climate Change*. Cambridge University Press.

McGregor, D. A., Harris, W. B., Dietl, G. P., & Kelley, P. (2011). Strontium isotopic dating of the Waccamaw Formation at Acme, NC, and the Duplin Formation at Tar Heel, NC: A Plio-Pleistocene research progress report. *Geological Society of America Abstracts with Programs*, *43*(2), 4.

Moat, J., & Du Puy, D. (2010). *Simplified Geology of Madagascar* [Map]. Royal Botanic Gardens, Kew. https://databasin.org/datasets/1a187e2f29e24e98b2c4d45c109d3bb3/

Morlighem, M., Williams, C. N., Rignot, E., An, L., Arndt, J. E., Bamber, J. L., Catania, G., Chauché, N., Dowdeswell, J. A., Dorschel, B., Fenty, I., Hogan, K., Howat, I., Hubbard, A., Jakobsson, M., Jordan, T. M., Kjeldsen, K. K., Millan, R., Mayer, L., … Zinglersen, K. B. (2017). BedMachine v3: Complete Bed Topography and Ocean Bathymetry Mapping of Greenland From Multibeam Echo Sounding Combined With Mass Conservation. *Geophysical Research Letters*, *44*(21), 11,051-11,061. https://doi.org/10.1002/2017GL074954

Moucha, R., Forte, A. M., Mitrovica, J. X., Rowley, D. B., Quéré, S., Simmons, N. A., & Grand, S. P. (2008). Dynamic topography and long-term sea-level variations: There is no such thing as a stable continental platform. *Earth and Planetary Science Letters*, *271*(1), 101–108. https://doi.org/10.1016/j.epsl.2008.03.056

Moucha, R., & Ruetenik, G. A. (2017). Interplay between dynamic topography and flexure along the U.S. Atlantic passive margin: Insights from landscape evolution modeling. *Global and Planetary Change*, *149*, 72–78. https://doi.org/10.1016/j.gloplacha.2017.01.004

Moulik, P., & Ekström, G. (2014). An anisotropic shear velocity model of the Earth's mantle using normal modes, body

waves, surface waves and long-period waveforms. *Geophysical Journal International*, *199*(3), 1713–1738. https://doi.org/10.1093/gji/ggu356

870   Muhs, D. R. (2022). MIS 5e sea-level history along the Pacific coast of North America. *Earth System Science Data*, *14*(3), 1271–1330. https://doi.org/10.5194/essd-14-1271-2022

Nairn, A. E. M., & Stehli, F. G. (Eds.). (1982). *The Ocean Basins and Margins*. Springer US. https://doi.org/10.1007/978-1-4615-8038-6

Ni, S., Tan, E., Gurnis, M., & Helmberger, D. (2002). Sharp Sides to the African Superplume. *Science*, *296*(5574), 1850

875   –1852. https://doi.org/10.1126/science.1070698

Peltier, W. R. (2004). GLOBAL GLACIAL ISOSTASY AND THE SURFACE OF THE ICE-AGE EARTH: The ICE-5G (VM2) Model and GRACE. *Annual Review of Earth and Planetary Sciences*, *32*(1), 111–149. https://doi.org/10.1146/annurev.earth.32.082503.144359

Persits, F. M., Ahlbrandt, T. S., Tuttle, M. L., Charpentier, R. R., Brownfield, M. E., & Takahashi, K. I. (1997). Maps

880   showing geology, oil and gas fields and geological provinces of Africa [USGS Numbered Series]. In *Maps showing geology, oil and gas fields and geological provinces of Africa* (Vols. 97-470-A). U.S. Geological Survey. https://doi.org/10.3133/ofr97470A

Péwé, T. L. (1975). *Quaternary Geology of Alaska*. U.S. Government Printing Office (USGS).

Pik, R., Bellahsen, N., Leroy, S., Denèle, Y., Razin, P., Ahmed, A., & Khanbari, K. (2013). Structural control of basement

885   denudation during rifting revealed by low-temperature (U–Th–Sm)/He thermochronology of the Socotra Island basement—Southern Gulf of Aden margin. *Tectonophysics*, *607*, 17–31. https://doi.org/10.1016/j.tecto.2013.07.038

Pirmez, C., Pratson, L. F., & Steckler, M. S. (1998). Clinoform development by advection-diffusion of suspended sediment: Modeling and comparison to natural systems. *Journal of Geophysical Research: Solid Earth*, *103*(B10), 24141–24157. https://doi.org/10.1029/98JB01516

890   Platel, J. P., Philip, J., Bourdillon-de-Grissac, C., Babinot, J. F., Roger, J., & Mercadier, C. (1994). Modalites de la transgression campanienne sur le massif du Haushi-Huqf (Oman); stratigraphie, contexte geodynamique et paleoenvironnements. *Bulletin de La Société Géologique de France*, *165*(2), 147–161.

Raymo, M. E., Kozdon, R., Evans, D., Lisiecki, L., & Ford, H. L. (2018). The accuracy of mid-Pliocene δ18O-based ice volume and sea level reconstructions. *Earth-Science Reviews*, *177*, 291–302.

895   https://doi.org/10.1016/j.earscirev.2017.11.022

Raymo, M. E., Mitrovica, J. X., O'Leary, M. J., DeConto, R. M., & Hearty, P. J. (2011). Departures from eustasy in Pliocene sea-level records. *Nature Geoscience*, *4*(5), 328–332. https://doi.org/10.1038/ngeo1118

Raymond, O., Liu, S., Gallagher, R., Zhang, W., & Highet, L. (2012). *Surface Geology of Australia, 1:1 million scale dataset, 2012 edition* [Map].

900   Richards, F. D., Coulson, S. L., Hoggard, M. J., Austermann, J., Dyer, B., & Mitrovica, J. X. (2023). Geodynamically

corrected Pliocene shoreline elevations in Australia consistent with midrange projections of Antarctic ice loss. *Science Advances*, *9*(46), eadg3035. https://doi.org/10.1126/sciadv.adg3035

Richards, F. D., Hoggard, M. J., Ghelichkhan, S., Koelemeijer, P., & Lau, H. C. P. (2023). Geodynamic, geodetic, and seismic constraints favour deflated and dense-cored LLVPs. *Earth and Planetary Science Letters*, *602*, 117964. https://doi.org/10.1016/j.epsl.2022.117964

Richards, F. D., Hoggard, M. J., White, N., & Ghelichkhan, S. (2020). Quantifying the Relationship Between Short-Wavelength Dynamic Topography and Thermomechanical Structure of the Upper Mantle Using Calibrated Parameterization of Anelasticity. *Journal of Geophysical Research: Solid Earth*, *125*(9), e2019JB019062. https://doi.org/10.1029/2019JB019062

Ries, A. C., & Shackleton, R. M. (1990). Structures in the Huqf-Haushi Uplift, east Central Oman. *Geological Society, London, Special Publications*, *49*(1), 653–663. https://doi.org/10.1144/GSL.SP.1992.049.01.39

Ritsema, J., Deuss, A., van Heijst, H. J., & Woodhouse, J. H. (2011). S40RTS: A degree-40 shear-velocity model for the mantle from new Rayleigh wave dispersion, teleseismic traveltime and normal-mode splitting function measurements. *Geophysical Journal International*, *184*(3), 1223–1236. https://doi.org/10.1111/j.1365-246X.2010.04884.x

Roberts, G. G., & White, N. (2010). Estimating uplift rate histories from river profiles using African examples. *Journal of Geophysical Research: Solid Earth*, *115*(B2). https://doi.org/10.1029/2009JB006692

Robertson, A. H. F., Searle, M. P., & Ries, A. C. (Eds.). (1990). *The geology and tectonics of the Oman Region*. Geological Society.

Robinson, N., Regetz, J., & Guralnick, R. P. (2014). EarthEnv-DEM90: A nearly-global, void-free, multi-scale smoothed, 90m digital elevation model from fused ASTER and SRTM data. *ISPRS Journal of Photogrammetry and Remote Sensing*, *87*, 57–67. https://doi.org/10.1016/j.isprsjprs.2013.11.002

Rodríguez, Charles S. Morris, & J. Eric Belz. (2006). A Global Assessment of the SRTM Performance. *Photogrammetric Engineering and Remote Sensing*, *72*(3), 249–260. https://doi.org/10.14358/PERS.72.3.249

Rodríguez, E., Morris, C. S., Belz, J. E., Chapin, E. C., Martin, J. M., Daffer, W., & Hensley, S. (2005). *An Assessment of the SRTM Topographic Products* (D-31639). Jet Propulsion Laboratory.

Rovere, A., Hearty, P. J., Austermann, J., Mitrovica, J. X., Gale, J., Moucha, R., Forte, A. M., & Raymo, M. E. (2015). Mid-Pliocene shorelines of the US Atlantic Coastal Plain—An improved elevation database with comparison to Earth model predictions. *Earth-Science Reviews*, *145*, 117–131. https://doi.org/10.1016/j.earscirev.2015.02.007

Rovere, A., Raymo, M. E., Mitrovica, J. X., Hearty, P. J., O'Leary, M. J., & Inglis, J. D. (2014). The Mid-Pliocene sea-level conundrum: Glacial isostasy, eustasy and dynamic topography. *Earth and Planetary Science Letters*, *387*, 27–33. https://doi.org/10.1016/j.epsl.2013.10.030

Rovere, A., Raymo, M. E., Vacchi, M., Lorscheid, T., Stocchi, P., Gómez-Pujol, L., Harris, D. L., Casella, E., O'Leary, M.

J., & Hearty, P. J. (2016). The analysis of Last Interglacial (MIS 5e) relative sea-level indicators: Reconstructing sea-level in a warmer world. *Earth-Science Reviews*, *159*, 404–427. https://doi.org/10.1016/j.earscirev.2016.06.006

Schaeffer, A. J., & Lebedev, S. (2013). Global shear speed structure of the upper mantle and transition zone. *Geophysical Journal International*, *194*(1), 417–449. https://doi.org/10.1093/gji/ggt095

Schlüter, T. (Ed.). (2006). Socotra (Yemen). In *Geological Atlas of Africa: With Notes on Stratigraphy, Tectonics, Economic Geology, Geohazards and Geosites of Each Country* (pp. 206–207). Springer. https://doi.org/10.1007/3-540-29145-8_50

Shakun, J. D., Lea, D. W., Lisiecki, L. E., & Raymo, M. E. (2015). An 800-kyr record of global surface ocean δ18O and implications for ice volume-temperature coupling. *Earth and Planetary Science Letters*, *426*, 58–68. https://doi.org/10.1016/j.epsl.2015.05.042

Shennan, I. (2015). Handbook of sea-level research. In *Handbook of Sea-Level Research* (pp. 3–25). John Wiley & Sons, Ltd. https://doi.org/10.1002/9781118452547.ch2

Simmons, N. A., Forte, A. M., & Grand, S. P. (2007). Thermochemical structure and dynamics of the African superplume. *Geophysical Research Letters*, *34*(2). https://doi.org/10.1029/2006GL028009

Simmons, N. A., Forte, A. M., & Grand, S. P. (2009). Joint seismic, geodynamic and mineral physical constraints on three-dimensional mantle heterogeneity: Implications for the relative importance of thermal versus compositional heterogeneity. *Geophysical Journal International*, *177*(3), 1284–1304. https://doi.org/10.1111/j.1365-246X.2009.04133.x

Spratt, R. M., & Lisiecki, L. E. (2016). A Late Pleistocene sea level stack. *Climate of the Past*, *12*(4), 1079–1092. https://doi.org/10.5194/cp-12-1079-2016

Steinberger, B. (2016). Topography caused by mantle density variations: Observation-based estimates and models derived from tomography and lithosphere thickness. *Geophysical Journal International*, *205*(1), 604–621. https://doi.org/10.1093/gji/ggw040

Tackley, P. J. (2008). Modelling compressible mantle convection with large viscosity contrasts in a three-dimensional spherical shell using the yin-yang grid. *Physics of the Earth and Planetary Interiors*, *171*(1), 7–18. https://doi.org/10.1016/j.pepi.2008.08.005

Tawadros, E. (2001). *Geology of Egypt and Libya*. A.A. Balkema.

Tawadros, E. (2011). *Geology of North Africa*. CRC Press.

Till, A. D., Dumoulin, J. A., Werdon, M. B., & Bleick, H. A. (2009). *Preliminary Bedrock Geologic Map of the Seward Peninsula, Alaska, and Accompanying Conodont Data* [Map]. U.S. Geological Survery Open-File Report. https://pubs.usgs.gov/of/2009/1254/

Trenhaile, A. (2014). Modelling the effect of Pliocene–Quaternary changes in sea level on stable and tectonically active land masses. *Earth Surface Processes and Landforms*, *39*(9), 1221–1235. https://doi.org/10.1002/esp.3574

van de Plassche, O. (2013). *Sea-level research: A manual for the collection and evaluation of data: A manual for the*

collection and evaluation of data. Springer.

Winker, C. D., & Howard, J. D. (1977). Correlation of tectonically deformed shorelines on the southern Atlantic coastal plain. *Geology*, *5*(2), 123–127. https://doi.org/10.1130/0091-7613(1977)5<123:COTDSO>2.0.CO;2

Yamauchi, H., & Takei, Y. (2016). Polycrystal anelasticity at near-solidus temperatures. *Journal of Geophysical Research: Solid Earth*, *121*(11), 7790–7820. https://doi.org/10.1002/2016JB013316

Yang, T., & Gurnis, M. (2016). Dynamic topography, gravity and the role of lateral viscosity variations from inversion of global mantle flow. *Geophysical Journal International*, *207*(2), 1186–1202. https://doi.org/10.1093/gji/ggw335

Zheng, L., Gordon, R. G., & Kreemer, C. (2014). Absolute plate velocities from seismic anisotropy: Importance of correlated errors. *Journal of Geophysical Research: Solid Earth*, *119*(9), 7336–7352. https://doi.org/10.1002/2013JB010902

Zhong, S., Gurnis, M., & Hulbert, G. (1993). Accurate determination of surface normal stress in viscous flow from a consistent boundary flux method. *Physics of the Earth and Planetary Interiors*, *78*(1), 1–8. https://doi.org/10.1016/0031-9201(93)90078-N